Article:
Parker, R.J., Nicholson, R.B. and Alcock, H.L. (2021) Far and extreme ultraviolet radiation fields and consequent disc destruction in star-forming regions. Monthly Notices of the Royal Astronomical Society, 502 (2). pp. 2665-2681. ISSN: 0035-8711

https://doi.org/10.1093/mnras/stab054

Monthly Notices
of the
ROYAL ASTRONOMICAL SOCIETY

MNRAS **502,** 2665–2681 (2021)
Advance Access publication 2021 January 11

doi:10.1093/mnras/stab054

Far and extreme ultraviolet radiation fields and consequent disc destruction in star-forming regions

Richard J. Parker ,★† Rhana B. Nicholson and Hayley L. Alcock

Department of Physics and Astronomy, The University of Sheffield, Hicks Building, Hounsfield Road, Sheffield S3 7RH, UK

Accepted 2020 December 18. Received 2020 December 18; in original form 2020 October 5

ABSTRACT

The first stages of planet formation usually occur when the host star is still in a (relatively) dense star-forming region, where the effects of the external environment may be important for understanding the outcome of the planet formation process. In particular, star-forming regions that contain massive stars have strong far-ultraviolet (FUV) and extreme ultraviolet (EUV) radiation fields, which can induce mass-loss from protoplanetary discs due to photoevaporation. In this paper, we present a parameter-space study of the expected FUV and EUV fields in *N*-body simulations of star-forming regions with a range of initial conditions. We then use recently published models to determine the mass-loss due to photoevaporation from protoplanetary discs. In particular, we focus on the effects of changing the initial degree of spatial structure and initial virial ratio in the star-forming regions, as well as the initial stellar density. We find that the FUV fields in star-forming regions are much higher than in the interstellar medium, even when the regions have stellar densities as low as in the Galactic field, due to the presence of intermediate-mass, and massive, stars ($>5\,\mathrm{M}_\odot$). These strong radiation fields lead to the destruction of the gas component in protoplanetary discs within 1 Myr, implying that gas giant planets must either form extremely rapidly (<1 Myr), or that they exclusively form in star-forming regions like Taurus, which contain no intermediate-mass or massive stars. The latter scenario is in direct tension with meteoritic evidence from the Solar system that suggests the Sun and its protoplanetary disc was born in close proximity to massive stars.

Key words: methods: numerical – protoplanetary discs – photodissociation region (PDR) – open clusters and associations: general.

1 INTRODUCTION

Most stars form in regions with tens to thousands of other stars where the stellar density of these groups exceeds the density of the Galactic field by at least several orders of magnitude (Korchagin et al. 2003; Lada & Lada 2003; Bressert et al. 2010). The majority of star-forming regions are short-lived, tending to disperse after around 10 Myr (e.g. Lada 2010; Chevance et al. 2020).

On similar time-scales, young stars in these regions are observed to host protoplanetary discs (Andre & Montmerle 1994; O'dell & Wen 1994; Mann et al. 2014; ALMA Partnership et al. 2015; Ansdell et al. 2017; van Terwisga, Hacar & van Dishoeck 2019), which are far more abundant at ages less than 5 Myr than at older ages (Haisch, Lada & Lada 2001; Richert et al. 2018). The reason for this observed depletion is likely to be a combination of rapid planet formation (Johansen et al. 2007), accretion on to the central star (Hartmann et al. 1998; Stamatellos, Whitworth & Hubber 2011), internally driven winds from the host star (e.g. Ercolano & Pascucci 2017), as well as destruction from external processes, such as truncation due to encounters with passing stars (Scally & Clarke 2001; Olczak, Pfalzner & Eckart 2008; Rosotti et al. 2014; Vincke, Breslau & Pfalzner 2015; Portegies Zwart 2016; Vincke & Pfalzner 2016; Winter et al. 2018a,b).

As well as truncation due to encounters with passing stars, discs can be destroyed by photoionizing radiation from massive stars ($>10\,\mathrm{M}_\odot$). The initial mass function predicts far more low-mass ($<1\,\mathrm{M}_\odot$) stars than massive stars (Kroupa 2002; Chabrier 2005; Maschberger 2013), but if a star-forming region contains 100s to 1000s of low-mass stars, then the formation of at least one or more massive stars is likely (Parker & Goodwin 2007; Nicholson & Parker 2017).

Massive stars produce both extreme ultraviolet (EUV) radiation, where the individual photon energies are $h\nu > 13.6$ eV, and far-ultraviolet (FUV) radiation, where the individual photon energies are in the range $6 < h\nu \leq 13.6$ eV. Many authors have demonstrated that both forms of radiation are extremely destructive to the gaseous component of protoplanetary discs (Johnstone, Hollenbach & Bally 1998; Henney & O'Dell 1999; Störzer & Hollenbach 1999; Armitage 2000; Hollenbach, Yorke & Johnstone 2000; Scally & Clarke 2001; Adams et al. 2004; Winter et al. 2018b; Nicholson et al. 2019; Concha-Ramírez et al. 2019b; Haworth et al. 2021). Unless the dust particles are particularly small, in which case they can be entrained in the photoevaporative wind (Miotello et al. 2012), the dust content of the disc is largely unscathed by photoionizing radiation (Haworth et al. 2018a; Sellek, Booth & Clarke 2020).

Recently, Haworth et al. (2018b) introduced a new set of models for calculating the mass-loss from protoplanetary discs due to

★ E-mail: r.parker@sheffield.ac.uk
† Royal Society Dorothy Hodgkin Fellow.

photoevaporation caused by FUV radiation. The FRIED grid (Haworth et al. 2018b) requires as an input the stellar mass, disc mass, disc radius, and ambient FUV radiation field, expressed in terms of the Habing (1968) unit, $G_0 = 1.8 \times 10^{-3}$ erg s^{-1} cm^{-2}, which is the underlying FUV flux in the interstellar medium. The output is a mass-loss, which can be used in a post-processing analysis of an N-body simulation to determine the impact of photoionizing radiation on discs in simulated star-forming regions.

Whilst several authors have used the FRIED grid to determine mass-loss due to photoevaporation in specific star-forming regions or planetary systems, (Haworth et al. 2018a; Winter et al. 2018b, 2019b; Concha-Ramírez et al. 2019b; Winter, Clarke & Rosotti 2019a), to our knowledge no comprehensive parameter space study has yet been carried out to calculate both the EUV and FUV flux in star-forming regions with realistic initial conditions (spatial and kinematic substructure, e.g. Cartwright & Whitworth 2004; Goodwin & Whitworth 2004; Parker et al. 2014b; Lomax, Bates & Whitworth 2018), and the effects of these radiation fields on protoplanetary discs in such star-forming regions. Fatuzzo & Adams (2008) determined the EUV and FUV fluxes in nearby star-forming regions, but these are largely devoid of massive stars (and may not be representative of all star formation, Kruijssen 2012). Winter et al. (2018b) considered more distant star-forming regions, but tailored the stellar content of their simulations to match those regions.

In this paper, we take a more general approach and calculate the EUV and FUV fluxes in star-forming regions with different initial densities, spatial and kinematic substructure, virial ratios and stellar mass. The paper is organized as follows. In Section 2, we describe our simulations, including the post-processing analysis we use to calculate the effects of the photoionizing radiation on protoplanetary discs. We present our results in Section 3, we provide a discussion in Section 4 and we conclude in Section 5.

2 METHOD

In this section we describe the set-up of N-body simulations used to model evolution of the star-forming regions, and we then describe the post-processing routine used to model photoevaporative mass-loss from protoplanetary discs.

2.1 Star-forming regions

For each set of initial conditions, we create 20 versions of the same simulation to gauge the effects of stochasticity on the results. Our default models contain $N = 1500$ stars, with masses drawn from a Maschberger (2013) IMF, which has a probability distribution of the form

$$p(m) \propto \left(\frac{m}{\mu}\right)^{-\alpha} \left(1 + \left(\frac{m}{\mu}\right)^{1-\alpha}\right)^{-\beta}. \quad (1)$$

Here, $\mu = 0.2\,\mathrm{M}_\odot$ is the average stellar mass, $\alpha = 2.3$ is the Salpeter (1955) power-law exponent for higher mass stars, and $\beta = 1.4$ describes the slope of the IMF for low-mass objects (which also deviates from the lognormal form; Bastian, Covey & Meyer 2010). We randomly sample this distribution in the mass range 0.1–50 $\mathrm{M}_\odot$, i.e. we do not include brown dwarfs in the simulations. Typically, for 1500 stars we draw between one and five massive ($>20\,\mathrm{M}_\odot$) stars for each realization of the simulation. We do not include primordial binary stars in the simulations; although binary stars are a common outcome of star formation (Raghavan et al. 2010; Duchêne & Kraus 2013), they complicate the formation, evolution, and stability of protoplanetary discs and so we defer their inclusion to a future paper.

In one set of simulations we keep the IMF constant so that we can isolate the effects of stochastically sampling the IMF from the stochastic dynamical evolution of the star-forming region. These simulations contain a 31 $\mathrm{M}_\odot$ star, an 18 $\mathrm{M}_\odot$ star, as well as around 10 stars with masses in the range 5–15 $\mathrm{M}_\odot$.

In another set of simulations, we draw $N = 150$ stars from the IMF. Statistically, we expect fewer massive stars (both O-type and lower mass B-type stars) in these regions, and star-forming regions with this number of stars are much more common in the vicinity of the Sun. With fewer or no massive stars, these regions will have lower ionizing radiation fluxes and so we expect protoplanetary discs to be less affected by photoevaporation in these low-mass star-forming regions.

The star-forming regions are set up as fractals in an attempt to mimic the spatial and kinematic substructure observed in young star-forming regions (Gomez et al. 1993; Larson 1995; Cartwright & Whitworth 2004; Sánchez & Alfaro 2009; André et al. 2014; Hacar et al. 2016). We refer the interested reader to Goodwin & Whitworth (2004) and Parker et al. (2014b) for a comprehensive description of the fractal distributions we use here. In brief, we use the box fractal method, which proceeds by defining a 'parent' in the centre of a cube which has sides of length $N_{\rm div} = 2$, which then spawns $N_{\rm div}^3$ subcubes. Each of the subcubes contains a 'child' at its centre, and the construction of the fractal proceeds by determining which of the children become parents themselves. The probability that a child becomes a parent is given by $N_{\rm div}^{D-3}$, where D is the fractal dimension. In this scheme, the lower the fractal dimension, the fewer children becomes parents and so there is more substructure.

The velocities of the parent particles are drawn from a Gaussian distribution with mean zero, and the children inherit these velocities plus a small random component (the size of which scales as $N_{\rm div}^{D-3}$) that decreases with each subsequent generation of the fractal. This results in a kinematic distribution in which the stars on local scales have very similar velocities, whereas on larger scales the velocities between stars can be very different. In the box fractal method we adopt here, on scales of size L the velocities scale as $v(L) \propto L^{3-D}$, so for $D = 1.6$, $v(L) \propto L^{1.4}$ and for $D = 2.0$ $v(L) \propto L$. [Note that the Larson (1981) linewidth relation roughly scales as $v(L) \propto L^{0.38}$.]

We create fractals with three different amounts of substructure. In the first, the fractal dimension $D = 1.6$, which results in a high degree of substructure, and the stellar velocities are strongly correlated on local scales. Most of our simulations have $D = 2.0$, which is a moderate amount of spatial substructure with some correlation in the velocities of nearby stars. Finally, we run models with $D = 3.0$, which is a uniform sphere with minimal correlation in the stellar velocities.

Once the fractal star-forming regions have been created, we scale the velocities of the individual stars to a bulk virial ratio, $\alpha_{\rm vir} = \mathcal{K}/|\Omega|$, where $\mathcal{K}$ is the total kinetic energy and $|\Omega|$ is the total potential energy. Most young stars are observed to have subvirial velocities, so most of our simulations are scaled to $\alpha_{\rm vir} = 0.3$. This initiates a global collapse, although the time-scale on which this occurs depends on both the fractal dimension and the local stellar density. We also run simulations with $\alpha_{\rm vir} = 0.5$ (virial equilibrium) and $\alpha_{\rm vir} = 1.5$ (supervirial) to gauge the effects of the bulk motion of a star-forming region on the FUV and EUV fields, and subsequent photoevaporative mass-loss.

Finally, we vary the initial median stellar density in each star-forming region, by altering the radius of the fractal. We mostly use simulations with moderate substructure ($D = 2.0$) and subvirial

Table 1. A summary of the different initial conditions of our simulated star-forming regions. The columns show the number of stars, $N_{\rm stars}$, the initial radius of the star-forming region, r_F, the initial median local stellar density, $\tilde{\rho}$, the fractal dimension D, the initial virial ratio $\alpha_{\rm vir}$, and the variation of the Maschberger (2013, M13) IMF (either stochastic between the different realizations of the same simulation, or constant across all realizations).

$N_{\rm stars}$	r_F	$\tilde{\rho}$	D	$\alpha_{\rm vir}$	IMF
1500	1 pc	$1000\,{\rm M}_\odot\,{\rm pc}^{-3}$	2.0	0.3	M13, stochastic
1500	2.5 pc	$100\,{\rm M}_\odot\,{\rm pc}^{-3}$	2.0	0.3	M13, stochastic
1500	5.5 pc	$10\,{\rm M}_\odot\,{\rm pc}^{-3}$	2.0	0.3	M13, stochastic
1500	20 pc	$0.2\,{\rm M}_\odot\,{\rm pc}^{-3}$	2.0	0.3	M13, stochastic
1500	5 pc	$100\,{\rm M}_\odot\,{\rm pc}^{-3}$	1.6	0.3	M13, stochastic
1500	1.1 pc	$100\,{\rm M}_\odot\,{\rm pc}^{-3}$	3.0	0.3	M13, stochastic
1500	2.5 pc	$100\,{\rm M}_\odot\,{\rm pc}^{-3}$	2.0	0.5	M13, stochastic
1500	2.5 pc	$100\,{\rm M}_\odot\,{\rm pc}^{-3}$	2.0	1.5	M13, stochastic
1500	2.5 pc	$100\,{\rm M}_\odot\,{\rm pc}^{-3}$	2.0	0.3	M13, constant
150	0.75 pc	$100\,{\rm M}_\odot\,{\rm pc}^{-3}$	2.0	0.3	M13, stochastic

velocities ($\alpha_{\rm vir} = 0.3$), but for the comparison of the effect of changing the initial degree of substructure, we keep the median density constant and change the fractal dimension. In order to keep the stellar density constant, simulations with a high degree of substructure ($D = 1.6$) have a larger radius, r_F than simulations with no substructure ($D = 3.0$), because a high degree of substructure skews the median local density to higher values. We adopt four different initial local stellar densities, 1000, 100, 10, and $0.2\,{\rm M}_\odot\,{\rm pc}^{-3}$. The highest density is thought to be commensurate with the initial densities of regions such as the Orion Nebula Cluster (Parker 2014), whereas many star-forming regions are consistent with having lower densities (Parker & Alves de Oliveira 2017). Very diffuse stellar associations (such as Taurus or Cyg OB2) may have been low density at birth (e.g. $\sim 10\,{\rm M}_\odot\,{\rm pc}^{-3}$; Wright et al. 2014, 2016), and for completeness we run simulations where the stellar densities are similar to those in the Sun's local neighbourhood today (Korchagin et al. 2003).

We summarize the different combinations of parameters used as initial conditions for the simulations in Table 1.

The simulations are evolved for 10 Myr using the `kira` integrator within the `Starlab` environment (Portegies Zwart et al. 1999, 2001). We do not include stellar evolution in the simulations.

2.2 Disc photoevaporation and internal evolution

Directly including discs around stars in N-body simulations is too computationally prohibitive, especially in the non-equilibrium initial conditions we adopt for our star-forming regions (some attempts have been made to include discs in simulations using hybrid codes, e.g. Rosotti et al. 2014). In our simulations we model the discs and the mass-loss due to photoevaporation in a semi-analytical post-processing routine after the simulations have run (see also Scally & Clarke 2001; Adams et al. 2004; Winter et al. 2018b; Concha-Ramírez et al. 2019b; Nicholson et al. 2019, for a similar approach).

We set the initial disc mass to be 10 per cent of the host star's mass

$$M_{\rm disc} = 0.1\,M_\star, \tag{2}$$

which is higher than the minimum mass Solar Nebula (Hayashi 1981), but comfortably lower than the regime where the disc could become gravitationally unstable and fragment (Toomre 1964; Mayer et al. 2002; Meru 2015). We do not allow stars more massive than $3\,{\rm M}_\odot$ to host discs. Typically, out of 1500 stars in a simulation, around 1460 will host a disc, though this is subject to some scatter due to stochastic sampling of the IMF and the direct proportionality of disc mass to host star mass.

At each snapshot output of the simulation, we determine the distance of each disc-hosting star d to all stars more massive than $5\,{\rm M}_\odot$, which we adopt as the lowest mass star that emits far-ultraviolet (FUV) radiation. We then take the FUV and EUV luminosities, $L_{\rm FUV}$, $L_{\rm EUV}$, in Armitage (2000), which are calculated from stellar atmosphere models (Buser & Kurucz 1992; Schaller et al. 1992) and calculate the FUV and EUV flux for each star

$$F_{\rm FUV} = \frac{L_{\rm FUV}}{4\pi d^2}, \tag{3}$$

and

$$F_{\rm EUV} = \frac{L_{\rm EUV}}{4\pi d^2}. \tag{4}$$

In the subsequent analysis we retain the EUV flux in cgs units (${\rm erg\,s^{-1}\,cm^{-2}}$), but present the FUV flux in terms of the Habing (1968) unit, $G_0 = 1.8 \times 10^{-3}\,{\rm erg\,s^{-1}\,cm^{-2}}$, which is the background FUV flux in the interstellar medium.

In most simulations there is more than one star that emits FUV radiation (and often more than one star emitting EUV radiation), so we sum the fluxes from all of the emitting stars to obtain a total flux.

In addition to presenting the FUV and EUV fluxes for our different initial conditions for star-forming regions, we will also calculate the likely mass-loss due to photoevaporation in these FUV and EUV radiation fields. For EUV radiation, we adopt the mass-loss from Johnstone et al. (1998)

$$\dot{M}_{\rm EUV} \simeq 8 \times 10^{-12} r_{\rm disc}^{3/2} \sqrt{\frac{\Phi_i}{d^2}}\ {\rm M}_\odot\,{\rm yr}^{-1}. \tag{5}$$

Here, Φ_i is the ionizing EUV photon luminosity from each massive star in units of $10^{49}\,{\rm s}^{-1}$ and is dependent on the stellar mass according to the observations of Vacca, Garmany & Shull (1996) and Sternberg, Hoffmann & Pauldrach (2003). For example, a $41\,{\rm M}_\odot$ star has $\Phi = 10^{49}\,{\rm s}^{-1}$ and a $23\,{\rm M}_\odot$ star has $\Phi = 10^{48}\,{\rm s}^{-1}$. The disc radius $r_{\rm disc}$ is expressed in units of au and the distance to the massive star d is in pc.

To determine the photoevaporative mass-loss due to FUV radiation, we utilize the `FRIED` grid from Haworth et al. (2018b), which consists of a grid of mass-loss rates for given combinations of stellar mass, G_0, disc mass, disc radius, and disc surface density. We interpolate over the `FRIED` grid to choose most appropriate mass-loss value given an input of stellar mass, G_0, disc mass and disc radius.

We subtract mass from the discs according to the FUV-induced mass-loss rate in the `FRIED` grid and the EUV-induced mass-loss rate from equation (5). Models of mass-loss in discs usually assume the mass is removed from the edge of the disc (where the surface density is lowest) and we would expect the radius of the disc to decrease in this scenario. We employ a very simple way of reducing the radius by assuming the surface density of the disc at 1 au, $\Sigma_{1\,{\rm au}}$, from the host star remains constant during mass-loss (see also Haworth et al. 2018b; Haworth & Clarke 2019). If

$$\Sigma_{1\,{\rm au}} = \frac{M_{\rm disc}}{2\pi r_{\rm disc}[1\,{\rm au}]}, \tag{6}$$

where $M_{\rm disc}$ is the disc mass, and $r_{\rm disc}$ is the radius of the disc, then if the surface density at 1 au remains constant, a reduction in mass due to photoevaporation will result in the disc radius decreasing by

a factor equal to the disc mass decrease

$$r_{\rm disc}(t_k) = \frac{M_{\rm disc}(t_k)}{M_{\rm disc}(t_{k-1})} r_{\rm disc}(t_{k-1}). \quad (7)$$

Here, the radius after mass-loss, $r_{\rm disc}(t_k)$, is then a function of the radius before mass-loss, $r_{\rm disc}(t_{k-1})$, multiplied by the new disc mass ($M_{\rm disc}(t_k)$) divided by the previous disc mass ($M_{\rm disc}(t_{k-1})$).

The decrease in disc radius due to photoevaporation will be countered to some degree by expansion due to the internal viscous evolution of the disc. We implement viscous expansion by utilizing the diffusion equation (Lynden-Bell & Pringle 1974; Pringle 1981), with the parametrization given in Hartmann et al. (1998) and Hartmann (2009). In brief, the surface density Σ at a given radius R is

$$\Sigma = 1.4 \times 10^3 \frac{{\rm e}^{-R/(R_1 t_d)}}{(R/R_1) t_d^{3/2}} \left(\frac{M_{\rm disc}(0)}{0.1 {\rm M}_\odot}\right) \left(\frac{R_1}{10\,{\rm au}}\right)^{-2} {\rm g\,cm^{-2}}, \quad (8)$$

where $M_{\rm disc}(0)$ is the disc mass before viscous evolution and R_1 is a radial scaling factor, which we set as $R_1 = 10$ au. t_d is a non-dimensional time, such that at a given physical time t

$$t_d = 1 + \frac{t}{t_s}, \quad (9)$$

and the viscous time-scale, t_s is given by

$$t_s = 8 \times 10^4 \left(\frac{R_1}{10\,{\rm au}}\right) \left(\frac{\alpha}{10^{-2}}\right)^{-1} \left(\frac{M_\star}{0.5\,{\rm M}_\odot}\right)^{1/2} \left(\frac{T_{100\,{\rm au}}}{10\,{\rm K}}\right)^{-1} {\rm yr}. \quad (10)$$

Here, α is the disc viscosity parameter (Shakura & Sunyaev 1973) and $T_{100\,{\rm au}}$ is the temperature of the disc at a distance of 100 au from the star. We assume the temperature profile of the disc has the form

$$T(R) = T_{1\,{\rm au}} R^{-q}, \quad (11)$$

where $T_{1\,{\rm au}}$ is the temperature at 1 au from the host star and is derived from the stellar luminosity for pre-main sequence stars by Luhman et al. (2003b), Luhman (2004a), and Kirk & Myers (2011). We adopt $q = 0.5$ and $\alpha = 0.01$ (Hartmann et al. 1998).

Given the mass of the star, we calculate the temperature at 100 au and then calculate the viscous time-scale t_s. We then use this to calculate the surface density Σ as a function of radius R (equation 8), to determine the outer radius of the disc, $r_{\rm disc}$. We set the surface density threshold below which we consider the disc to be truncated, $R_{\rm trunc}$ to be 10^{-6} g cm^{-2}.

Following mass-loss due to photoevaporation and the subsequent inward movement of the disc radius according to equation (7), we calculate the change in truncation radius $R_{\rm trunc}(t_n)/R_{\rm trunc}(t_{n-1})$ and scale the disc radius $r_{\rm disc}$ accordingly

$$r_{\rm disc}(t_n) = r_{\rm disc}(t_{n-1}) \frac{R_{\rm trunc}(t_n)}{R_{\rm trunc}(t_{n-1})}. \quad (12)$$

(Note that the subscripts differ from those in equation 7 as they refer to different stages in the process; subscript $_k$ refers to the mass and radius before and after mass-loss due to photoevaporation, whereas subscript $_n$ refers to the mass and radius before and after viscous spreading and accretion on to the star.)

Finally, with viscous spreading in the disc we would expect some disc material to be accreted on to the host star. As our disc evolution occurs in a post-processing analysis, we do not add any extra mass to the star, but instead assume this extra mass is negligible compared to the stellar mass and merely subtract that mass from the disc itself, according to

$$M_{\rm disc}(t) = M_{\rm disc}(0) \left(1 + \frac{t}{t_s}\right)^{\frac{1}{2\gamma-4}}, \quad (13)$$

where $M_{\rm disc}(0)$ is the initial disc mass and $M_{\rm disc}(t)$ is the disc mass at time t, following viscous evolution, and the viscosity exponent γ is unity (Andrews et al. 2010).

As an example, for a 1 M$_\odot$ star with a $M_{\rm disc} = 0.1$ M$_\star$ disc with initial radius $r_{\rm disc} = 100$ au, after 0.1 Myr the disc will have a new radius $r_{\rm disc} = 173$ au and mass $M_{\rm disc} = 0.073$ M$_\star$. After 1 Myr the disc radius will be $r_{\rm disc} = 693$ au and mass $M_{\rm disc} = 0.032$ M$_\star$, and after 5 Myr the disc radius will be $r_{\rm disc} = 2314$ au and mass $M_{\rm disc} = 0.015$ M$_\star$. After 10 Myr of viscous evolution, the disc radius will be $r_{\rm disc} = 3826$ au and mass $M_{\rm disc} = 0.011$ M$_\star$. These values are similar to other analytical estimates (Hartmann 2009; Lichtenberg, Parker & Meyer 2016; Concha-Ramírez, Vaher & Portegies Zwart 2019a) as well as numerical simulations (Krumholz & Forbes 2015).

If the disc mass falls below zero, the disc is assumed to be destroyed and the star is denoted 'disc-less' [though in reality a significant amount of dust may still be present (Haworth et al. 2018a)]. The dynamical information (i.e. masses, positions, and velocities of the stars) is outputted every 0.1 Myr. However, in order to capture as much of the disc physics as possible we implement a much smaller time-step (10^{-3} Myr) for the disc mass-loss due to photoevaporation, and the internal viscous evolution. In Appendix A we demonstrate the effects of decreasing the timestep in the disc calculations.

3 RESULTS

In this section, we will describe the evolution of the FUV and EUV fluxes in star-forming regions with different initial conditions and then describe the mass-loss in discs due to photoevaporation in these radiation fields. Where we plot the evolution of the disc fraction in simulations, we show observed disc fractions in star-forming regions from Richert et al. (2018) for comparison (and these are shown by the dark grey points in the relevant figure panels). Note that we only implement viscous spreading in the simulation described in Section 3.3; all other models include inward evolution of the disc radius only.

3.1 FUV and EUV flux in a single star-forming region

In Fig. 1, we show the evolution of the FUV flux (G_0) in a subvirial ($\alpha_{\rm vir} = 0.3$), moderately substructured ($D = 2.0$) star-forming region with initial local stellar density $\tilde{\rho} = 100\,{\rm M}_\odot\,{\rm pc}^{-3}$. The median G_0 field (the solid black line) is initially $G_0 \sim 2000$, and this increases slightly as the star-forming region becomes more compact, before slowly decreasing (though it remains well above $G_0 = 100$, so the radiation field is more than 100 times that in the interstellar medium).

Across the simulation, there is a huge range in possible values (indicated by the dotted lines, which show the full range $G_0 = 100 - 10^7$ at the start of the simulation, and $G_0 = 1 - 10^6$ after 10 Myr). Interestingly, the G_0 field experienced by an individual star can hugely fluctuate, as shown by the coloured lines in Fig. 1.

3.2 Different initial conditions and ensembles of simulations

3.2.1 Stellar density

In Fig. 2, we vary the initial median local density in the star-forming region, while keeping the number of stars ($N = 1500$), virial ratio ($\alpha_{\rm vir} = 0.3$), and fractal dimension ($D = 2.0$) constant. The local stellar density is the mass volume density for each star ρ_{10}, where

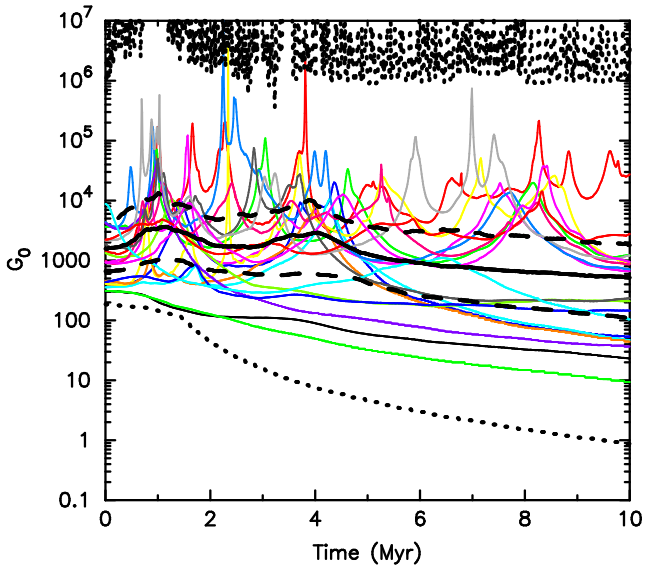

Figure 1. Evolution of the FUV flux in one simulated star-forming region where the initial local stellar density is $100\,\mathrm{M_\odot\,pc^{-3}}$. The solid black line shows the median G_0 value for all stars as a function of time, with the dashed lines indicating the interquartile range, and the dotted lines showing the full range. The G_0 values for 20 individual stars are shown by the coloured lines.

the volume is calculated to a fixed number of nearest neighbours (following Parker et al. 2014b we choose the tenth nearest neighbour, r_{10} but the results tend to be robust for any value in the range $N = 5-15$, Bressert et al. 2010; Parker & Meyer 2012), and the mass is the total mass of the 10 nearest neighbours, M_{10}:

$$\rho_{10} = \frac{3M_{10}}{4\pi r_{10}^3}. \tag{14}$$

We then take the median value of ρ_{10} to determine the median local density for each star-forming region, $\tilde{\rho}$. We show 20 versions of the same initial conditions, identical save for the random number seed used to initialize the mass functions, positions, and velocities of the stars.

In panels (a)–(d), we show the evolution of the median local stellar density by the coloured lines, as well as the mean density within the half-mass radius $\rho_{1/2}$ for all 20 simulations, shown by dot–dashed black line and defined as

$$\rho_{1/2} = \frac{3M_{F,1/2}}{4\pi r_{1/2}^3}, \tag{15}$$

where $M_{F,\,1/2}$ is half of the total stellar mass of the star-forming region, and $r_{1/2}$ is the radius from the centre that encloses this mass. In all the density regimes, the median local density is higher than the mean central density before dynamical evolution. As the star-forming regions undergo subvirial collapse, the central density can eventually exceed the initial local density.

This is seen in the evolution of the median FUV flux (second row, panels e–h) and the EUV flux (third row, panels i–l), which for the denser regions (the first two columns) have distinct peaks at the point where the region collapses to form a centrally concentrated, spherical star cluster at 1 Myr for the most dense regions ($\tilde{\rho} = 1000\,\mathrm{M_\odot\,pc^{-3}}$, panel e) and 3 Myr for regions with initial stellar densities of $\tilde{\rho} = 100\,\mathrm{M_\odot\,pc^{-3}}$ (panel f). There are also hints at a peak central density, indicative of a collapse, around or just after 10 Myr in the the simulations that start with median local densities of $\tilde{\rho} = 10\,\mathrm{M_\odot\,pc^{-3}}$ (the third column, panels g and k). The reasons for this behaviour are two-fold. First, the disc-hosting low-mass stars are being funnelled into the potential well of the cluster, so they are more likely to be close to the most massive stars. Secondly, the most massive stars undergo dynamical mass segregation (McMillan, Vesperini & Portegies Zwart 2007; Moeckel & Bonnell 2009; Allison et al. 2010), which increases the FUV and EUV flux experienced by the majority of the low-mass stars.

There is more variation in the EUV flux values between simulations than the FUV flux (compare e.g. panel g with panel k in Fig. 2), and this is due to the stochastic sampling of the IMF and the fact that the EUV flux comes from more massive (rarer) stars than the equivalent FUV flux.

In the most dense star-forming regions ($\tilde{\rho} = 1000\,\mathrm{M_\odot\,pc^{-3}}$), the initial FUV flux is $G_0 \sim 10^4$, which increases to $G_0 \sim 10^5$ during the formation of the cluster and subsequent mass segregation. Strikingly, the peak median G_0 value decreases by the same order of magnitude as the decrease in stellar density, so the simulations with stellar densities similar to the Galactic field ($0.2\,\mathrm{M_\odot\,pc^{-3}}$) still have G_0 values between 10 and 100 (panel h), i.e. between 10 and 100 times the FUV flux in the interstellar medium.

The high FUV and EUV fluxes, even at lower densities, have severely detrimental effects on the survival of the gas content within protoplanetary discs. When we implement the FRIED grid of photoevaporation models, we see a significant depletion in discs with initial radii of more than 10 au. Panels (m)–(p) show the fraction of stars that host protoplanetary discs with initial radii $r_{\rm disc} = 10$ au in each of the 20 simulations as a function of time. This fraction rapidly drops to 60 per cent in the densest simulations ($\tilde{\rho} = 1000\,\mathrm{M_\odot\,pc^{-3}}$), with final fractions between 10 to 50 per cent. As the stellar density (and G_0 fields) decrease, the fraction of surviving discs increases, as can be seen in panels (n)–(p), with almost no mass-loss due to photoevaporation in 10 au discs when the stellar density is field-like ($\tilde{\rho} = 0.2\,\mathrm{M_\odot\,pc^{-3}}$) and the G_0 fields are only a factor of 10–100 higher than the ISM (panel p).

However, when the disc radii are initially 100 au (with initial disc masses $0.1\,\mathrm{M_\star}$), the mass-loss due to photoevaporation is very drastic, with disc fractions dropping to between 0 and 50 per cent in the first 0.1 Myr, depending on the initial stellar density. If we take an example calculation from the FRIED grid, an average mass star ($0.5\,\mathrm{M_\odot}$) with a 100 au radius disc of mass $0.05\,\mathrm{M_\odot}$ in an FUV field of $G_0 = 100$ will experience a mass-loss rate of $\dot{M} = 1.43 \times 10^{-6}\,\mathrm{M_\odot\,yr^{-1}}$, i.e. will lose $0.143\,\mathrm{M_\odot}$ in 0.1 Myr. It is therefore unsurprising that we see such significant disc depletion in our simulated star-forming regions when using these models. In Appendix A, we show further examples of the evolution of discs subject to mass-loss from the FRIED grid.

3.2.2 *Initial spatial structure*

In Fig. 3, we show the effects of varying the initial degree of substructure by changing the fractal dimension of the star-forming regions. We fix the median local density to be $\tilde{\rho} = 100\,\mathrm{M_\odot\,pc^{-3}}$ in each simulation, which means the initial radii are quite different; $r_F = 5$ pc for the highly substructured simulations ($D = 1.6$), $r_F = 2.5$ pc for the moderately substructured simulations ($D = 2.0$) and $r_F = 1.1$ pc for the non-substructured simulations ($D = 3.0$). In this figure, the left-hand column shows the results for simulations with a high degree of substructure ($D = 1.6$) and the right-hand column shows the results for simulations with no substructure ($D = 3.0$). In each panel, the results from simulations with an intermediate amount of substructure ($D = 2.0$), but otherwise identical initial conditions, are shown by the background grey lines.

These very different initial radii affect the global evolution of the star-forming regions. The gravitational potential is $\psi \propto M_F/r_F$,

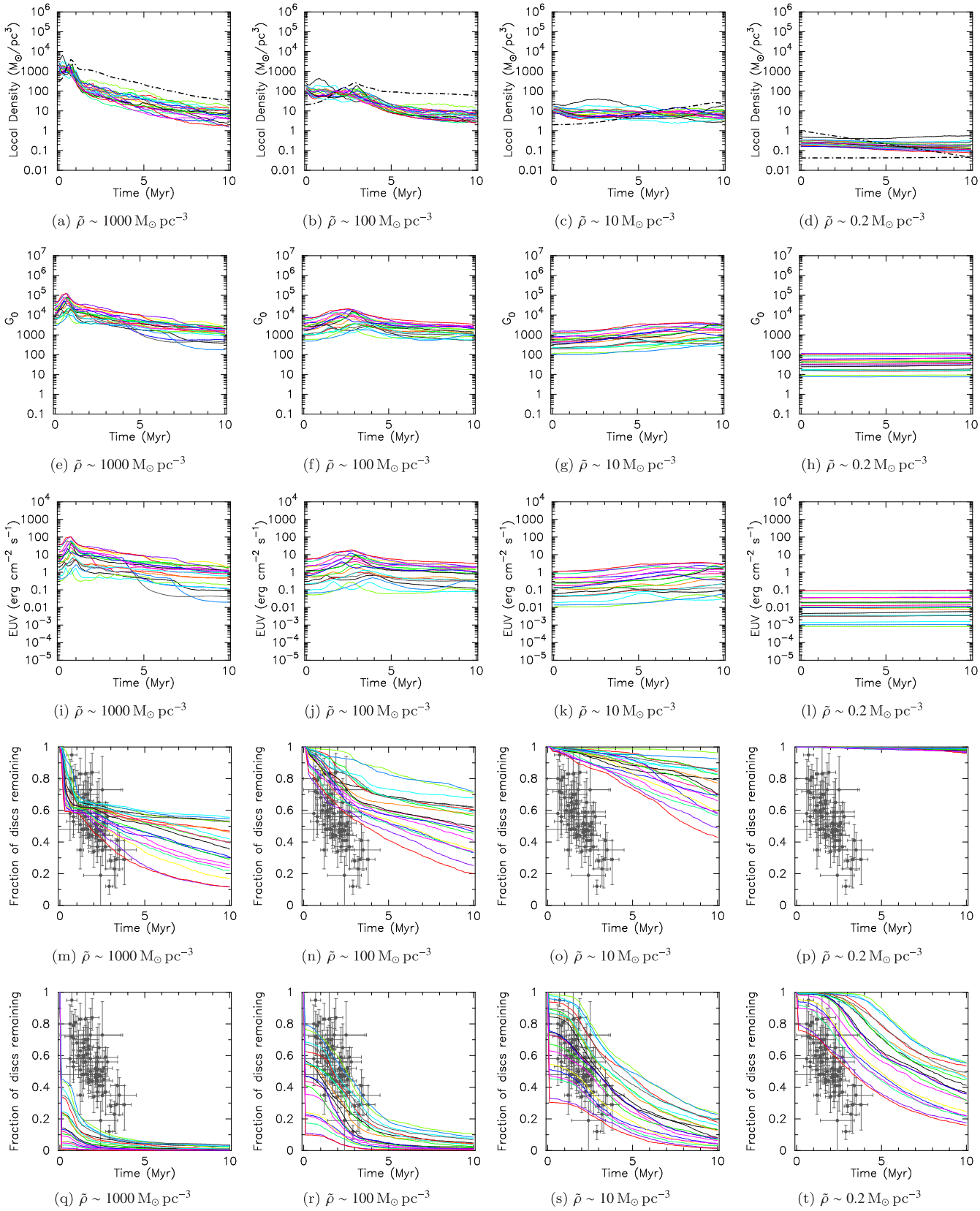

Figure 2. The effect of varying the initial local stellar density (the volume density within a sphere that encompasses the 10 nearest neighbours to each star). The top row shows the median local density in 20 realizations of the same star-forming region (indicated by the different coloured lines), as well as the mean density within the half-mass radius in all 20 simulations (the dot–dashed line). The second row shows the median FUV flux, G_0, in each simulation and the third row shows the median EUV flux. The fourth row shows the fraction of stars that host gaseous discs in each simulation, where the initial disc radius was 10 au; the fifth row shows the disc fraction when the initial disc radii were set to 100 au. These simulations do not include viscous evolution of the discs. The observed disc fractions in star-forming regions from Richert et al. (2018) are shown by the dark grey points.

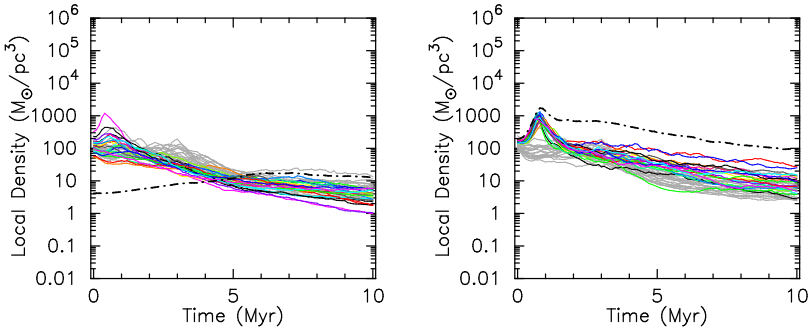

(a) $D = 1.6$ (b) $D = 3.0$

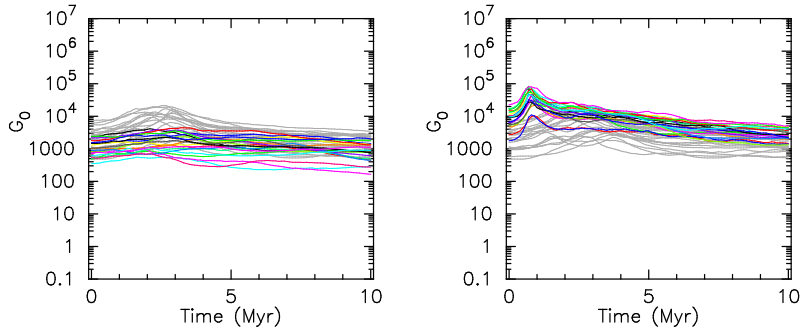

(c) $D = 1.6$ (d) $D = 3.0$

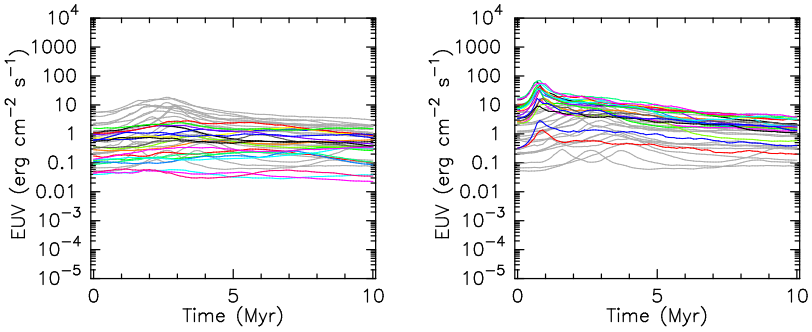

(e) $D = 1.6$ (f) $D = 3.0$

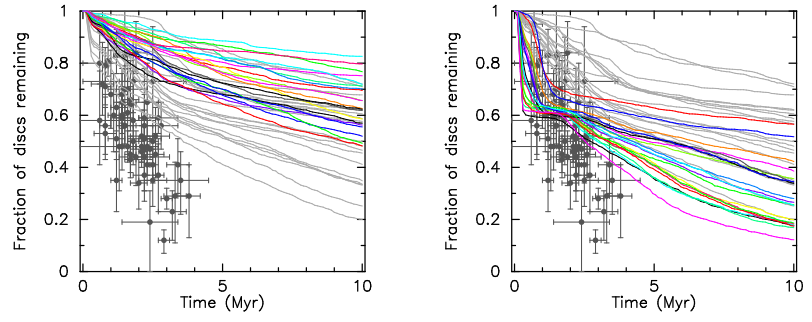

(g) $D = 1.6$ (h) $D = 3.0$

Figure 3. Comparison of the evolution of star-forming regions with different fractal dimensions but with constant initial stellar density ($\tilde{\rho} \sim 100\,\mathrm{M}_\odot\,\mathrm{pc}^{-3}$). The top row shows the median local density in 20 realizations of the same star-forming region (indicated by the different coloured lines), as well as the mean density within the half-mass radius in all 20 simulations (the dot–dashed line). The second row shows the median FUV flux, G_0, in each simulation and the third row shows the median EUV flux. The fourth row shows the fraction of stars that host gaseous discs in each simulation, where the initial disc radius was 10 au. The simulations with a high fractal dimension (less spatial and kinematic substructure) have higher G_0 values as the simulation progresses, because the substructure does not dynamically evolve, but the region collapses to form a cluster faster than the substructured regions (because the overall density is higher to begin with). The grey lines are the default simulations (moderate substructure, $D = 2.0$). The observed disc fractions in star-forming regions from Richert et al. (2018) are shown by the dark grey points.

where M_F and r_F are the mass and radius of the star-forming region, respectively. Therefore, a region with a smaller radius will have a deeper gravitational potential, which facilitates a deeper collapse of a subvirial star-forming region.

This is seen in the evolution of the central density of our star-forming regions, shown in panels (a) and (b) of Fig. 3. These three regions all have the same local stellar density (which reflects the density in the substructure), but the high degree of clumpiness for the regions with a low fractal dimension ($D = 1.6$, panel a) results in a large amount of empty space. Despite the common initial stellar density, the regions with no substructure (panel b) initially are able to collapse into a deeper potential well, and attain both local and central densities of $\tilde{\rho} = 1000\,\mathrm{M_\odot\,pc^{-3}}$, i.e. a factor of 10 higher than the initial density.

This behaviour significantly affects the radiation fields. First, the higher the substructure, the lower the initial G_0 and EUV fields. This is because the photoionizing stars are on average further away from the majority of stars than is the case for a uniform sphere (no substructure). Secondly, because the regions with no substructure can collapse to higher central densities (where the massive stars are located), the G_0 field reaches a maximum of nearly $G_0 = 10^5$ after the region collapses to form a cluster (panel d). Contrast this with the region with a high degree of initial substructure ($D = 1.6$), where the G_0 field remains constant at $G_0 = 1000$ for the entirety of the simulation (panel c). This behaviour is also the same for the EUV radiation fields.

The impact of the higher G_0 and EUV fields in the less substructured simulations can be seen in the evolution of the disc fractions for discs with initial radii $r_{\rm disc} = 10$ au (the trends are also similar for discs with larger radii, which we do not show here). The disc fractions in the simulations with $D = 1.6$ (substructured) drop to between 50 and 80 per cent, whereas in the simulations with no initial substructure the disc fractions drop to between 10 and 60 per cent.

Note that if these regions had similar initial *volume averaged densities* (equation 15), then the radii of the highly substructured ($D = 1.6$) simulations would be smaller, and in that case the more substructured regions would likely lead to more disc destruction than in the smoother regions. However, it is the *local* density the more accurately traces the dynamical evolution of these star-forming regions (Parker 2020), despite this not being commonly adopted by observers or simulators to characterize the density of star-forming regions.

Interestingly, the simulations with no initial substructure, shown in panel (h), display a flattening of the disc fractions after ∼0.5 Myr, before decreasing again. Here, the initial radiation field rapidly destroys discs in the first 0.5 Myr, but then as the central densities of the star-forming regions increase further disc destruction occurs. This behaviour is not present in the substructured simulations because the density of (and hence FUV fields within) the star-forming regions are highest at $t = 0$ Myr.

3.2.3 *Initial virial ratio*

We vary the initial virial ratio of the star-forming regions to determine the effect of the bulk motion on the survival of protoplanetary discs. Many star-forming regions are observed to be subvirial, which means they may collapse to form a bound cluster, but observations indicate that most star-forming regions have dispersed after 10 Myr. It is unclear what the main mechanism for dispersal is, but many authors have investigated the hypothesis that regions disperse with supervirial velocities, following the rapid removal of the gas potential leftover from the star formation process (Tutukov 1978; Lada, Margulis & Dearborn 1984; Goodwin 1997; Goodwin & Bastian 2006; Baumgardt & Kroupa 2007; Pfalzner & Kaczmarek 2013; Shukirgaliyev et al. 2018).

We mimic this process by setting our initial velocities to be supervirial initially, as well as running a set of simulations where the star-forming region is in global virial equilibrium. In Fig. 4, panel (a) we see that the density evolution of virialized star-forming regions (the coloured lines) is very similar to the subvirial regions (our default simulations, shown by the grey lines), apart from the subvirial regions attain higher central densities due to the more violent nature of the collapse. As we would expect, the supervirial regions (panel b) expand rapidly to low densities.

Interestingly, the different virial ratios lead to little variation in the radiation fields. The subvirial and virial regions tend to have slightly higher G_0 and EUV fields after 1 Myr (panel c and panel e), with quite similar fractions of surviving discs (panel g of Fig. 4). The supervirial regions have high G_0 values to begin with, and this largely governs the disc fractions over time, as most of the mass-loss due to photoevaporation occurs in the first 0.5 Myr. However, the G_0 and EUV fields are only a factor of 10 lower than in the (sub)virial regions after 10 Myr, despite the local density in the supervirial star-forming regions being a factor of 100 lower than at birth. The reason for this is that supervirial star-forming regions dynamically evolve so that the most massive stars sweep up retinues of low-mass stars (Parker et al. 2014b; Rate, Crowther & Parker 2020), meaning that the most massive stars will almost exclusively reside in the denser locations of the star-forming regions, where there are lots of low-mass stars that will experience strong radiation fields. However, there are also many low-mass stars that do not reside near to massive stars and so the fraction of discs that survive in supervirial regions can be 25 per cent higher than in the (sub)virial star-forming region (compare the coloured lines with the grey lines in panel h).

3.2.4 *IMF sampling and low* N

We now take our default simulation ($\tilde{\rho} \sim 100\,\mathrm{M_\odot\,pc^{-3}}$, $D = 2.0$, $\alpha_{\rm vir} = 0.3$) and remove the variation of the stellar IMF between different realizations of the same simulation. We adopt a single IMF, and the only parameters that vary randomly are the positions and velocities of the individual stars. We show the results of this in the left-hand column of Fig. 5. The grey lines show the values from the default simulation, where the numbers of massive stars are allowed to vary between simulations with statistically the same initial conditions.

Whilst the evolution of the local density varies between the different simulations, the spread in G_0 and EUV fields is noticeably narrower than in the simulations where the IMF varies between realizations. This also leads to a narrower range of disc fractions, suggesting it is not the individual dynamics of statistically similar star-forming regions that dominates disc photoevaporation, but rather the mass distribution of stars.

We further demonstrate this point by examining the photoevaporation in star-forming regions with only $N = 150$ stars (but again, with initial densities of $\tilde{\rho} \sim 100\,\mathrm{M_\odot\,pc^{-3}}$). These regions expand faster than the higher mass regions, but it is striking that there is a significant spread in the G_0 and EUV fields. This is because the IMF is not fully sampled; in some instances the region contains several stars above $5\,\mathrm{M_\odot}$ that produce radiation fields, but in two of our simulations no such stars are produced. Of the regions that do contain photoionizing stars, the median G_0 fields range from $G_0 = 10$ to $G_0 = 10^4$. This translates into a huge range in the fractions of surviving discs, from 100 per cent in the simulations with no intermediate or massive stars,

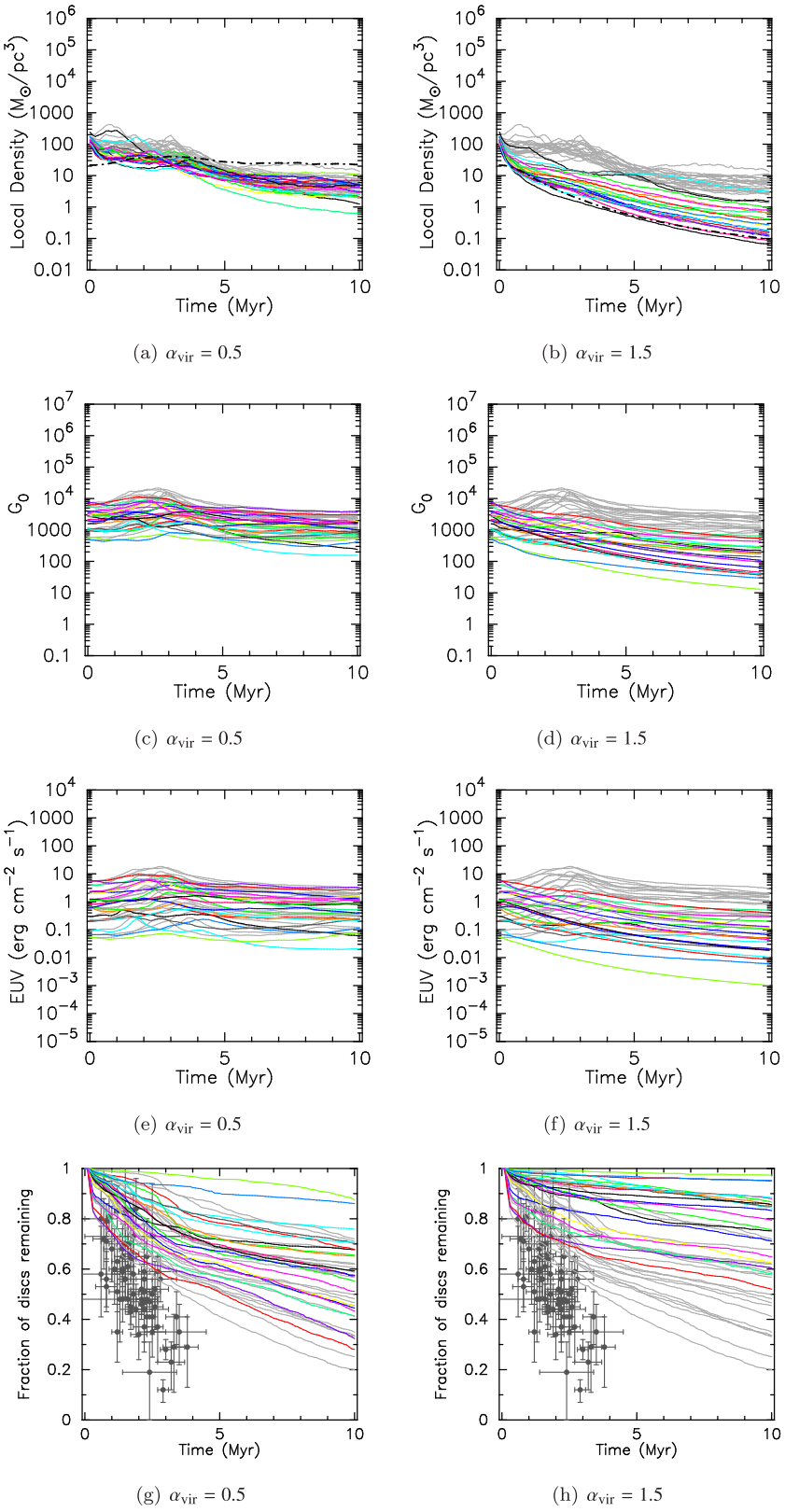

(a) $\alpha_{\rm vir} = 0.5$ (b) $\alpha_{\rm vir} = 1.5$

(c) $\alpha_{\rm vir} = 0.5$ (d) $\alpha_{\rm vir} = 1.5$

(e) $\alpha_{\rm vir} = 0.5$ (f) $\alpha_{\rm vir} = 1.5$

(g) $\alpha_{\rm vir} = 0.5$ (h) $\alpha_{\rm vir} = 1.5$

Figure 4. The effect of varying the initial virial ratios when the initial stellar density is kept constant ($\tilde{\rho} \sim 100\,{\rm M}_\odot\,{\rm pc}^{-3}$). We also use the same initial fractal dimension ($D = 2.0$). The top row shows the median local density in 20 realizations of the same star-forming region (indicated by the different coloured lines), as well as the mean density within the half-mass radius in all 20 simulations (the dot–dashed line). The second row shows the median FUV flux, G_0, in each simulation and the third row shows the median EUV flux. The fourth row shows the fraction of stars that host gaseous discs in each simulation, where the initial disc radius was 10 au. The left-hand column shows simulations where the initial virial ratio is $\alpha_{\rm vir} = 0.5$ (virial equilibrium). The right-hand column shows simulations where the initial virial ratio is $\alpha_{\rm vir} = 1.5$ (supervirial). The default simulations, which are subvirial ($\alpha_{\rm vir} = 0.3$), are shown by the background grey lines. The observed disc fractions in star-forming regions from Richert et al. (2018) are shown by the dark grey points.

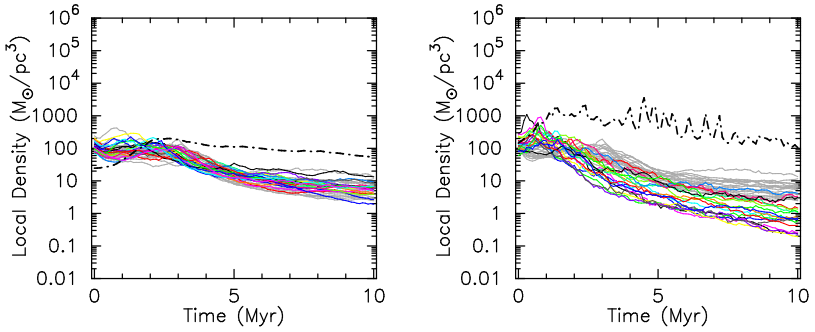

(a) Constant mass function, $N = 1500$ (b) Stochastic IMF sampling, $N = 150$

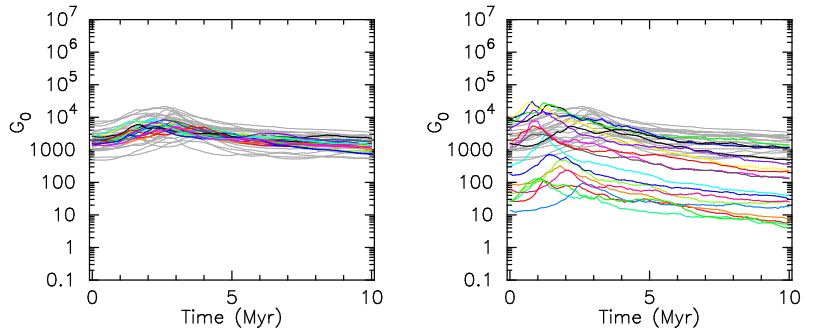

(c) Constant mass function, $N = 1500$ (d) Stochastic IMF sampling, $N = 150$

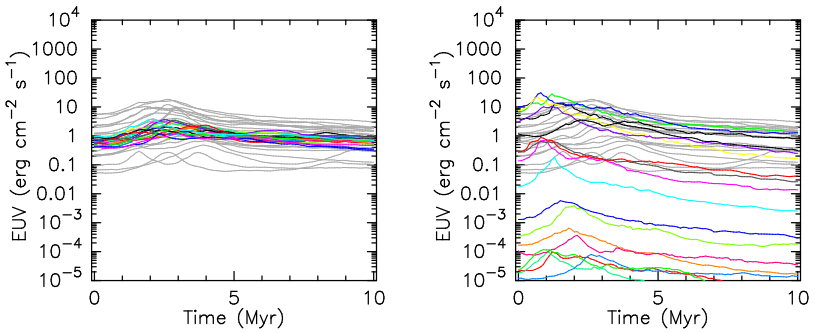

(e) Constant mass function, $N = 1500$ (f) Stochastic IMF sampling, $N = 150$

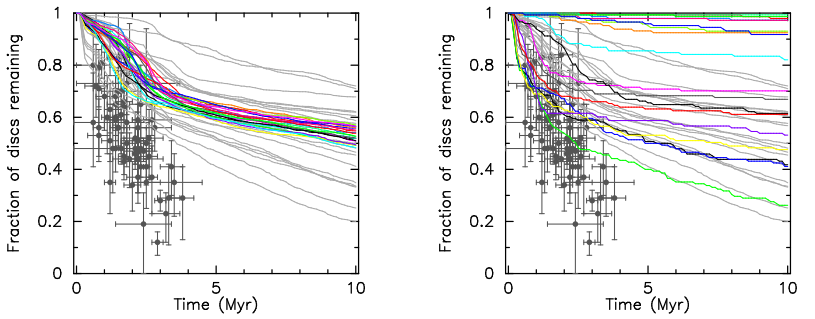

(g) Constant mass function, $N = 1500$ (h) Stochastic IMF sampling, $N = 150$

Figure 5. Comparison of different mass distributions with constant initial stellar density ($\tilde{\rho} \sim 100\,\mathrm{M}_\odot\,\mathrm{pc}^{-3}$). The top row shows the median local density in 20 realizations of the same star-forming region (indicated by the different coloured lines), as well as the mean density within the half-mass radius in all 20 simulations (the dot–dashed line). The second row shows the median FUV flux, G_0, in each simulation and the third row shows the median EUV flux. The fourth row shows the fraction of stars that host gaseous discs in each simulation, where the initial disc radius was 10 au. The left-hand column shows the results for simulations that are identical to our default simulation ($\alpha_{\rm vir} = 0.3$, $D = 2.0$, $N = 1500$, $r_F = 2.5\,\mathrm{pc}$), but where the mass distribution of stars is identical in each simulation (whereas the positions and velocities of the stars are randomly different). The right-hand panel shows simulations with our default density, virial ratio, and degree of substructure, but now the total number of stars is only $N = 150$. The grey lines indicate the results for our default simulations. The observed disc fractions in star-forming regions from Richert et al. (2018) are shown by the dark grey points.

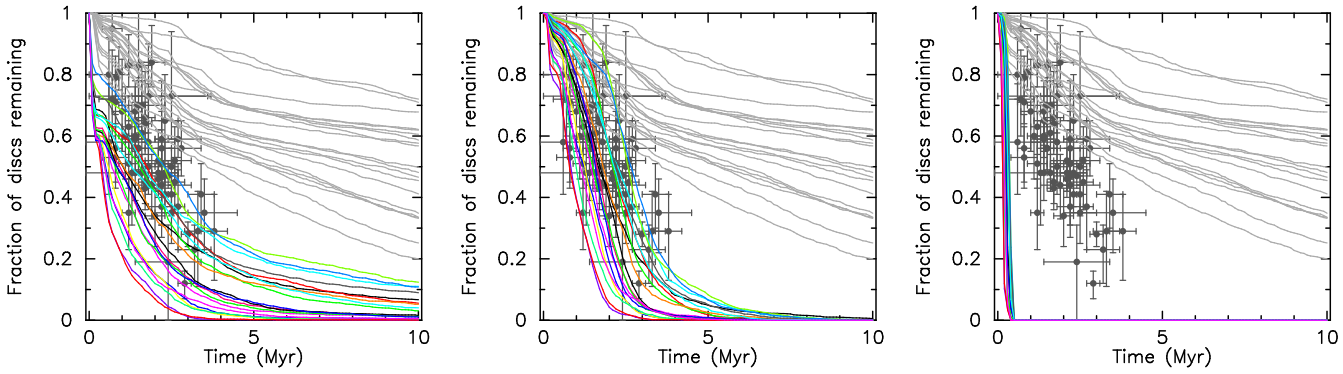

(a) Radius fixed to initial value

(b) Evolving disc radius, viscous evolution

(c) Evolving disc radius, viscous evolution, accretion onto central star

Figure 6. The evolution of discs in our default simulation ($\tilde{\rho} \sim 100\,\mathrm{M_\odot\,pc^{-3}}$, $D = 2.0$, $\alpha_{\rm vir} = 0.3$) where the initial disc radii are all 10 au. In panel (a), we show the fraction of discs over time following mass-loss due to photoevaporation, but the radius is kept constant. The grey lines indicate the disc fractions when the disc radius is allowed to decrease. In panel (b), the disc radii are allowed to decrease during photoevaporation (by keeping the surface density of the disc at 1 au constant), and then increase again due to viscous spreading. In panel (c), we also allow mass-loss in the inner edge of the disc due to accretion on to the central star. The grey lines indicate the results for our default simulations. The observed disc fractions in star-forming regions from Richert et al. (2018) are shown by the dark grey points.

to 83 per cent in a simulation that only contains a $6\,\mathrm{M_\odot}$ star, to as low as 25 per cent for a region containing stars with masses 14, 19, and $44\,\mathrm{M_\odot}$.

3.3 Viscous evolution in discs

Until now the only internal disc evolution we have included is the disc's response to losing mass through photoevaporation. We have fixed the surface density of the disc to be constant at 1 au from the star, so that when the disc loses mass the radius must decrease. In Fig. 6(a) we show the evolution of the disc fraction in our default simulation ($\tilde{\rho} \sim 100\,\mathrm{M_\odot\,pc^{-3}}$, $D = 2.0$, $\alpha_{\rm vir} = 0.3$) but we do not allow the outer radius to evolve inwards. Instead, the outer radius is set to be constant, and the result is a much more rapid destruction of the discs (compare the coloured lines with the grey lines, which are discs with the same initial radius, but whose radii evolve inwards in the same simulations Fig. 2n).

We then allow the radius to evolve inwards due to the disc preferentially losing material from its edges during photoevaporation (as in our default calculations), but this time we implement viscous spreading in the disc, so that the outer radius can increase. This viscous spreading causes the fraction of discs to drop significantly, because the discs have lower mass (due to the photoevaporative mass-loss), and an increased radius and reduced mass makes the disc even more susceptible to further mass-loss. This is shown in Fig. 6(b), where the disc fractions decrease to zero after ∼6 Myr. At first glance, the combination of photoevaporation and viscous evolution appears to reproduce the observed disc fractions extremely well. However, if we also allow mass-loss due to accretion on to the central star from the inner edge of the disc, then the discs are depleted on much faster time-scales (∼0.5 Myr, see Fig. 6c) because their further mass-loss makes them more susceptible to subsequent future photoevaporation.

We emphasize that our analytical method to model the viscous evolution of the discs may not capture all of the physics in a full simulation (Krumholz & Forbes 2015), but in this regard it is no worse than our prescription for the mass-loss due to photoevaporation, which is essentially an interpolation of more complex simulation results (Haworth et al. 2018b). The point is that viscous spreading would increase the radius of the disc, thereby lowering the surface density and making the disc more susceptible to mass-loss due to photoevaporation.

4 DISCUSSION

As one would expect, in our simulations the radiation field is lower for star-forming regions with similar stellar populations but with lower densities. Our simulation parameter space encompasses very dense ($\tilde{\rho} = 1000\,\mathrm{M_\odot\,pc^{-3}}$) regions, all the way down to regions with densities similar to the Galactic field (∼$0.2\,\mathrm{M_\odot\,pc^{-3}}$; Korchagin et al. 2003). Due to the presence of massive stars, the FUV flux in our simulations exceeds the FUV flux in the interstellar medium, G_0 (Habing 1968), by a factor of 10–100. This means that in any star-forming region with stars $>10\,\mathrm{M_\odot}$, the environment experienced by a protoplanetary disc is much more destructive than in a star-forming region without massive stars (e.g. Taurus; Luhman et al. 2003a; Luhman 2004b; Güdel et al. 2007).

Fatuzzo & Adams (2008) calculated the FUV flux for star-forming regions in the solar neighbourhood, and due to the dearth of massive stars in these nearby regions, obtained fluxes that are considerably lower than those we find in our simulations. Our calculated FUV and EUV fluxes are probably more appropriately compared to the Orion Nebula Cluster, which contains several stars above $20\,\mathrm{M_\odot}$. This then poses the interesting question of what star-forming region did the Sun (and other extrasolar planet host stars) form in – if massive stars were present in these regions during planet formation, then the EUV and FUV fluxes will have been much higher than in the nearby star-forming regions we observe today.

Interestingly, even a low-mass star-forming region (i.e. $N = 150$ stars) will still have a large EUV and FUV flux if it contains any massive stars. This is shown in the right-hand panel of Fig. 5, where the EUV and FUV fluxes are comparable to those in much more populous star-forming regions. In fact, some low-mass regions have higher FUV and EUV fluxes than more populous regions, simply due to their having more massive stars. If the mass functions of the regions are set to be constant, there is very little variation in the FUV and EUV fluxes between simulations with the same initial stellar densities.

The most notable result in our parameter space study is how effective FUV radiation is at destroying discs. The FRIED grid simulations from Haworth et al. (2018b) predict the almost total destruction of $r_{\rm disc} = 100$ au discs within less than 1 Myr. When the initial disc radius is set to just 10 au, photoevaporation still leads to the destruction of at least 45 per cent of discs (and sometimes much more) in the most dense star-forming regions ($\tilde{\rho} = 1000\,{\rm M}_{\odot}\,{\rm pc}^{-3}$).

The FRIED models tend to be more destructive than earlier models of disc mass-loss due to photoevaporation (Scally & Clarke 2001; Nicholson et al. 2019), and we compare the disc fractions between the FRIED grid and the earlier models in Appendix B. These models have the same prescription for mass-loss due to EUV radiation, so the only difference is in the mass-loss due to FUV radiation.

An implication of this rapid destruction of protoplanetary disc is that gas giant planets like Jupiter and Saturn must have to form close to their host star because discs with radii >10 au do not survive in our simulations, and within 1–2 Myr (cf. Nicholson et al. 2019), which appears to be corroborated by recent observational studies that find evidence for extremely rapid planet formation (Alves et al. 2020; Segura-Cox et al. 2020). Alternatively, perhaps gas giant planets exclusively form in star-forming regions where there are no massive stars. This latter hypothesis is however in tension with the idea that the Sun formed in the vicinity of massive stars that enriched the Sun's protoplanetary disc (or protosolar nebula) in the short-lived radioisotopes ^{26}Al and ^{60}Fe (Adams 2010; Gounelle & Meynet 2012; Adams, Fatuzzo & Holden 2014; Parker et al. 2014a; Lichtenberg et al. 2016; Nicholson & Parker 2017; Lichtenberg et al. 2019).

In our simulations, the initial stellar density is the most important factor in determining if a disc will be destroyed. As Fig. 2 shows, usually more than 50 per cent of 10 au discs are destroyed in the most dense regions, whereas in very low density regions almost all of these discs survive.

There is considerable debate in the literature as to the initial density of star-forming regions, as several authors have pointed out that the present-day density cannot be reliably used as a proxy for the initial density (Marks & Kroupa 2012; Parker 2014). However, a combination of different structural and kinematic analyses seems to suggest that most star-forming regions probably have initial densities of at least $\tilde{\rho} = 100\,{\rm M}_{\odot}\,{\rm pc}^{-3}$ (Parker 2014; Wright et al. 2014; Parker & Alves de Oliveira 2017; Schoettler et al. 2020). If we adopt an initial density of $\tilde{\rho} = 100\,{\rm M}_{\odot}\,{\rm pc}^{-3}$ as our 'default' density, then we would expect between 20 to 70 per cent of 10 au discs to survive after a few Myr, but 100 au discs would almost all be destroyed. The implication of this is that if gas giant planets are forming in environments that contain massive stars, they need to form in the inner (sub-10 au) regions of discs, but presumably further out than the snow/ice line(s).

Varying the other initial conditions besides stellar density generally results in only a minimal difference to the fraction of surviving discs. In particular, despite the expansion in supervirial simulations, most of the discs are destroyed early on, when the star-forming region is still compact. The degree of initial spatial and kinematic substructure can affect the fraction of surviving discs. Simulations with less substructure have a more uniform density profile than substructured regions (even though the median *initial* stellar density is the same), and therefore the stars are on average closer to more of the ionizing stars. This results in more photoevaporation of the discs, and additionally, the non-substructured regions have a smaller radius and therefore deeper gravitational potential during the subvirial collapse, leading to higher central densities and further destruction of the discs.

In most of our calculations we have not included the effects of viscous evolution, and instead have just adjusted the radius of the disc so that it evolves inwards following mass-loss due to photoevaporation (Haworth & Clarke 2019). When we include viscous evolution, the disc radius is first adjusted inwards and we then calculate the subsequent expansion of the disc due to viscous evolution. Although the outer radius tends to increase by only a small amount during this viscous spreading, the disc is more susceptible to photoevaporation because its mass and therefore surface density have decreased.

Our implementation of viscous evolution is purely analytical and may be too simplistic, but appears to be in reasonable agreement with simulations conducted with the VADER code (Krumholz & Forbes 2015; Concha-Ramírez et al. 2019b), as well as other analytical estimates (Hartmann et al. 1998; Lichtenberg et al. 2016; Concha-Ramírez et al. 2019a).

While it is not the intention of this paper to attempt to match the disc fractions for individual star-forming regions, we show the observed disc fractions in nearby star-forming regions from Richert et al. (2018) in our plots. A general comparison should not be made between the observations and our simulations because the observed regions in the Richert et al. (2018) data may have different initial stellar densities from one another, as well as different disc radii (both in terms of the present-day and initial radii).

However, we may draw some tentative conclusions. First, if the disc radius decreases due to photoevaporation, and viscous evolution does not subsequently increase the radius, too many discs survive if their initial radii are 10 au. However, if viscous evolution is effective, then the disc fractions in our simulations match those in the observational data in regions with initial stellar densities of $\tilde{\rho} = 100\,{\rm M}_{\odot}\,{\rm pc}^{-3}$ (compare the grey lines to the coloured lines, and the observational data, in Fig. 6b), with the caveat that accretion of mass on to the central star would also increase the rate of photoevaporation (Fig. 6c).

Discs with larger initial radii (100 au) lose mass much more rapidly, and the disc fractions in these simulations match the observed fractions in regions with initial stellar densities of $\tilde{\rho} = 10\,{\rm M}_{\odot}\,{\rm pc}^{-3}$. Future numerical work could in principle be tailored to specific star-forming regions to test the initial disc radius distributions, and the role of different internal physics (e.g. viscous evolution) on the evolution of the discs.

5 CONCLUSIONS

We have performed *N*-body simulations of the dynamical evolution of star-forming regions with a wide range of initial conditions. We have varied the initial stellar density, degree of spatial and kinematic substructure, virial ratio and initial mass distribution. We then calculated the the FUV and EUV fluxes within these star-forming regions and used these to determine the mass-loss due to photoevaporation from protoplanetary discs within these regions. Our conclusions are the following.

(i) In all of our star-forming regions, the FUV flux is significantly higher than the value measured in the interstellar medium ($G_0 = 1.8 \times 10^{-3}$ erg s^{-1} cm^{-2}). Even when our simulations start with stellar densities similar to the Galactic field ($0.1\,{\rm M}_{\odot}\,{\rm pc}^{-3}$), the FUV flux can be as high as $100\,G_0$. This is caused by the presence of massive stars, and even regions with intermediate-mass (B-type stars, 5–15 M$_{\odot}$) experience very high radiation fields.

(ii) We determine the mass-loss in protoplanetary discs due to external radiation fields by using the new FRIED grid of photoevaporative mass-loss models (Haworth et al. 2018b). In the radiation fields present in our star-forming regions, mass-loss due to

photoevaporation would destroy the gas component of discs if those discs have radii of more than 10 au.

(iii) Whilst the initial stellar density is the biggest factor in determining the fate of the discs, subtle changes to the initial conditions of star-forming regions with identical initial densities can also affect the survival chances of discs. Star-forming regions with low levels of spatial and kinematic substructure lead to a more uniform, and longer lasting exposure, to radiation fields from massive stars. This leads to more discs being destroyed. The overall bulk motion of the region, set by the initial virial ratio, has a much more minimal affect of the fraction of surviving discs.

(iv) If we implement a simple prescription of the viscous evolution of the discs, then the outward spreading of the disc radius, combined with mass accretion on to the central star, severely exacerbates the destruction of discs.

(v) Taken together, this suggests that gas giant planets such as Jupiter and Saturn must either form extremely rapidly (<1 Myr – for recent observational evidence see Alves et al. 2020; Segura-Cox et al. 2020, and for further theoretical evidence see also Concha-Ramírez et al. 2019b; Nicholson et al. 2019), and relatively close to the parent star (i.e. beyond the snow line, but within 10 au of the star), or these planets exclusively form in star-forming regions like Taurus where there are no photoionizing sources.

(vi) The latter scenario is in significant tension with the evidence from short-lived radioisotopes (SLRs) in meteorites that suggest that the Sun formed in a star-forming region that contained one or more massive stars that enriched the Sun's protoplanetary disc (Ouellette, Desch & Hester 2007; Parker et al. 2014a; Lichtenberg et al. 2016; Nicholson & Parker 2017), or the prestellar core from which the Sun formed (Gounelle & Meynet 2012). Further investigation is required to determine whether a Solar system analogue can survive photoevaporative mass-loss *and* be enriched in SLRs.

ACKNOWLEDGEMENTS

We are grateful to the anonymous referee for their prompt, constructive and helpful reports. RJP acknowledges support from the Royal Society in the form of a Dorothy Hodgkin Fellowship. HLA was supported by the 2018 Sheffield Undergraduate Research Experience (SURE) scheme.

DATA AVAILABILITY STATEMENT

The data used to produce the plots in this paper will be shared on reasonable request to the corresponding author.

REFERENCES

Adams F. C., 2010, ARA&A, 48, 47
Adams F. C., Hollenbach D., Laughlin G., Gorti U., 2004, ApJ, 611, 360
Adams F. C., Fatuzzo M., Holden L., 2014, ApJ, 789, 86
Allison R. J., Goodwin S. P., Parker R. J., Portegies Zwart S. F., de Grijs R., 2010, MNRAS, 407, 1098
ALMA Partnership et al., 2015, ApJ, 808, L3
Alves F. O., Cleeves L. I., Girart J. M., Zhu Z., Franco G. A. P., Zurlo A., Caselli P., 2020, ApJ, 904, L6
Andre P., Montmerle T., 1994, ApJ, 420, 837
André P., Di Francesco J., Ward-Thompson D., Inutsuka S.-I., Pudritz R. E., Pineda J. E., 2014, Protostars and Planets VI. Univ. Arizona Press, Tucson, AZ, p. 27
Andrews S. M., Wilner D. J., Hughes A. M., Qi C., Dullemond C. P., 2010, ApJ, 723, 1241
Ansdell M., Williams J. P., Manara C. F., Miotello A., Facchini S., van der Marel N., Testi L., van Dishoeck E. F., 2017, AJ, 153, 240
Armitage P. J., 2000, A&A, 362, 968
Bastian N., Covey K. R., Meyer M. R., 2010, ARA&A, 48, 339
Baumgardt H., Kroupa P., 2007, MNRAS, 380, 1589
Bressert E. et al., 2010, MNRAS, 409, L54
Buser R., Kurucz R. L., 1992, A&A, 264, 557
Cartwright A., Whitworth A. P., 2004, MNRAS, 348, 589
Chabrier G., 2005, in Corbelli E., Palla F., Zinnecker H., eds, The Initial Mass Function 50 Years Later, Vol. 327, Springer, Dordrecht, p. 41
Chevance M. et al., 2020, MNRAS, 493, 2872
Concha-Ramírez F., Vaher E., Portegies Zwart S., 2019a, MNRAS, 482, 732
Concha-Ramírez F., Wilhelm M. J. C., Portegies Zwart S., Haworth T. J., 2019b, MNRAS, 490, 5678
Duchêne G., Kraus A., 2013, ARA&A, 51, 269
Ercolano B., Pascucci I., 2017, R. Soc. Open Sci., 4, 170114
Fatuzzo M., Adams F. C., 2008, ApJ, 675, 1361
Gomez M., Hartmann L., Kenyon S. J., Hewitt R., 1993, AJ, 105, 1927
Goodwin S. P., 1997, MNRAS, 286, 669
Goodwin S. P., Bastian N., 2006, MNRAS, 373, 752
Goodwin S. P., Whitworth A. P., 2004, A&A, 413, 929
Gounelle M., Meynet G., 2012, A&A, 545, A4
Güdel M. et al., 2007, A&A, 468, 353
Habing H. J., 1968, BAIN, 19, 421
Hacar A., Alves J., Forbrich J., Meingast S., Kubiak K., Großschedl J., 2016, A&A, 589, A80
Haisch Jr. K. E., Lada E. A., Lada C. J., 2001, ApJ, 553, L153
Hartmann L., 2009, Accretion Processes in Star Formation, 2nd edn. Cambridge Univ. Press, Cambridge
Hartmann L., Calvet N., Gullbring E., D'Alessio P., 1998, ApJ, 495, 385
Haworth T. J., Clarke C. J., 2019, MNRAS, 485, 3895
Haworth T. J., Facchini S., Clarke C. J., Mohanty S., 2018a, MNRAS, 475, 5460
Haworth T. J., Clarke C. J., Rahman W., Winter A. J., Facchini S., 2018b, MNRAS, 481, 452
Haworth T. J., Kim J. S., Winter A. J., Hines D. C., Clarke C. J., Sellek A. D., Ballabio G., Stapelfeldt K. R., 2021, MNRAS, 501, 3502
Hayashi C., 1981, Prog. Theor. Phys. Suppl., 70, 35
Henney W. J., O'Dell C. R., 1999, AJ, 118, 2350
Hollenbach D. J., Yorke H. W., Johnstone D., 2000, Protostars and Planets IV. Univ. Arizona Press, Tucson, AZ, p. 401
Johansen A., Oishi J. S., Mac Low M.-M., Klahr H., Henning T., Youdin A., 2007, Nature, 448, 1022
Johnstone D., Hollenbach D., Bally J., 1998, ApJ, 499, 758
Kirk H., Myers P. C., 2011, ApJ, 727, 64
Korchagin V. I., Girard T. M., Borkova T. V., Dinescu D. I., van Altena W. F., 2003, AJ, 126, 2896
Kroupa P., 2002, Science, 295, 82
Kruijssen J. M. D., 2012, MNRAS, 426, 3008
Krumholz M. R., Forbes J. C., 2015, Astron. Comput., 11, 1
Lada C. J., 2010, R. Soc. London Phil. Trans. Ser. A, 368, 713
Lada C. J., Lada E. A., 2003, ARA&A, 41, 57
Lada C. J., Margulis M., Dearborn D., 1984, ApJ, 285, 141
Larson R. B., 1981, MNRAS, 194, 809
Larson R. B., 1995, MNRAS, 272, 213
Lichtenberg T., Parker R. J., Meyer M. R., 2016, MNRAS, 462, 3979
Lichtenberg T., Golabek G. J., Burn R., Meyer M. R., Alibert Y., Gerya T. V., Mordasini C., 2019, Nat. Astron., 3, 307
Lomax O., Bates M. L., Whitworth A. P., 2018, MNRAS, 480, 371
Luhman K. L., 2004a, ApJ, 602, 816
Luhman K. L., 2004b, ApJ, 617, 1216
Luhman K. L., Briceño C., Stauffer J. R., Hartmann L., Barrado y Navascués D., Caldwell N., 2003a, ApJ, 590, 348
Luhman K. L., Stauffer J. R., Muench A. A., Rieke G. H., Lada E. A., Bouvier J., Lada C. J., 2003b, ApJ, 593, 1093
Lynden-Bell D., Pringle J. E., 1974, MNRAS, 168, 603
McMillan S. L. W., Vesperini E., Portegies Zwart S. F., 2007, ApJ, 655, L45
Mann R. K. et al., 2014, ApJ, 784, 82

Marks M., Kroupa P., 2012, A&A, 543, A8
Maschberger T., 2013, MNRAS, 429, 1725 (M13)
Mayer L., Quinn T., Wadsley J., Stadel J., 2002, Science, 298, 1756
Meru F., 2015, MNRAS, 454, 2529
Miotello A., Robberto M., Potenza M. A. C., Ricci L., 2012, ApJ, 757, 78
Moeckel N., Bonnell I. A., 2009, MNRAS, 396, 1864
Nicholson R. B., Parker R. J., 2017, MNRAS, 464, 4318
Nicholson R. B., Parker R. J., Church R. P., Davies M. B., Fearon N. M., Walton S. R. J., 2019, MNRAS, 485, 4893
O'dell C. R., Wen Z., 1994, ApJ, 436, 194
Olczak C., Pfalzner S., Eckart A., 2008, A&A, 488, 191
Ouellette N., Desch S. J., Hester J. J., 2007, ApJ, 662, 1268
Parker R. J., 2014, MNRAS, 445, 4037
Parker R. J., 2020, R. Soc. Open Sci., 7, 201271
Parker R. J., Alves de Oliveira C., 2017, MNRAS, 468, 4340
Parker R. J., Goodwin S. P., 2007, MNRAS, 380, 1271
Parker R. J., Meyer M. R., 2012, MNRAS, 427, 637
Parker R. J., Church R. P., Davies M. B., Meyer M. R., 2014a, MNRAS, 437, 946
Parker R. J., Wright N. J., Goodwin S. P., Meyer M. R., 2014b, MNRAS, 438, 620
Pfalzner S., Kaczmarek T., 2013, A&A, 555, A135
Portegies Zwart S. F., 2016, MNRAS, 457, 313
Portegies Zwart S. F., Makino J., McMillan S. L. W., Hut P., 1999, A&A, 348, 117
Portegies Zwart S. F., McMillan S. L. W., Hut P., Makino J., 2001, MNRAS, 321, 199
Pringle J. E., 1981, ARA&A, 19, 137
Raghavan D. et al., 2010, ApJSS, 190, 1
Rate G., Crowther P. A., Parker R. J., 2020, MNRAS, 495, 1209
Richert A. J. W., Getman K. V., Feigelson E. D., Kuhn M. A., Broos P. S., Povich M. S., Bate M. R., Garmire G. P., 2018, MNRAS, 477, 5191
Rosotti G. P., Dale J. E., de Juan Ovelar M., Hubber D. A., Kruijssen J. M. D., Ercolano B., Walch S., 2014, MNRAS, 441, 2094
Salpeter E. E., 1955, ApJ, 121, 161
Sánchez N., Alfaro E. J., 2009, ApJ, 696, 2086
Scally A., Clarke C., 2001, MNRAS, 325, 449
Schaller G., Schaerer D., Meynet G., Maeder A., 1992, A&AS, 96, 269
Schoettler C., de Bruijne J., Vaher E., Parker R. J., 2020, MNRAS, 495, 3104
Segura-Cox D. M. et al., 2020, Nature, 586, 228
Sellek A. D., Booth R. A., Clarke C. J., 2020, MNRAS, 492, 1279
Shakura N. I., Sunyaev R. A., 1973, A&A, 500, 33
Shukirgaliyev B., Parmentier G., Just A., Berczik P., 2018, ApJ, 863, 171
Stamatellos D., Whitworth A. P., Hubber D. A., 2011, ApJ, 730, 32
Sternberg A., Hoffmann T. L., Pauldrach A. W. A., 2003, ApJ, 599, 1333
Störzer H., Hollenbach D., 1999, ApJ, 515, 669
Toomre A., 1964, ApJ, 139, 1217
Tutukov A. V., 1978, A&A, 70, 57
Vacca W. D., Garmany C. D., Shull J. M., 1996, ApJ, 460, 914
van Terwisga S. E., Hacar A., van Dishoeck E. F., 2019, A&A, 628, A85
Vincke K., Pfalzner S., 2016, ApJ, 828, 48
Vincke K., Breslau A., Pfalzner S., 2015, A&A, 577, A115
Winter A. J., Clarke C. J., Rosotti G., Booth R. A., 2018a, MNRAS, 475, 2314
Winter A. J., Clarke C. J., Rosotti G., Ih J., Facchini S., Haworth T. J., 2018b, MNRAS, 478, 2700
Winter A. J., Clarke C. J., Rosotti G. P., 2019a, MNRAS, 485, 1489
Winter A. J., Clarke C. J., Rosotti G. P., Hacar A., Alexander R., 2019b, MNRAS, 490, 5478
Wright N. J., Parker R. J., Goodwin S. P., Drake J. J., 2014, MNRAS, 438, 639
Wright N. J., Bouy H., Drew J. E., Sarro L. M., Bertin E., Cuillandre J.-C., Barrado D., 2016, MNRAS, 460, 2593

APPENDIX A: SIMULATION RESOLUTION

Given the fast rate of destruction in our simulations, we deemed it prudent to check whether the time resolution of our simulations was adequate. For example, using a snapshot output of 0.1 Myr may be too coarse to determine the true effects of photoevaporation.

To determine the optimum time-step for calculating the disc evolution, we fix the snapshot output for the dynamical information from the *N*-body simulation to be 0.1 Myr (changing this time-scale makes no discernible difference to the G_0 values in the simulation). We then reduce the time-step of the disc evolution calculation (both mass-loss due to photoevaporation, and internal viscous evolution).

We show examples of the evolution of single discs in a fixed radiation field in Figs A1–A5. In each figure, we show the evolution of the disc mass in panel (a), the evolution of the disc radius according to equation (7) in panel (b), and the mass-loss rate that induces this disc evolution in panel (c). The mass-loss rates are not constant, even in a constant radiation field, because the `FRIED` grid provides mass-loss rates that depend on the disc mass and radius, as well as the radiation field. In all panels the coloured lines indicate different time-steps in the algorithm; 10^{-1} Myr (solid grey), 10^{-2} Myr (dashed

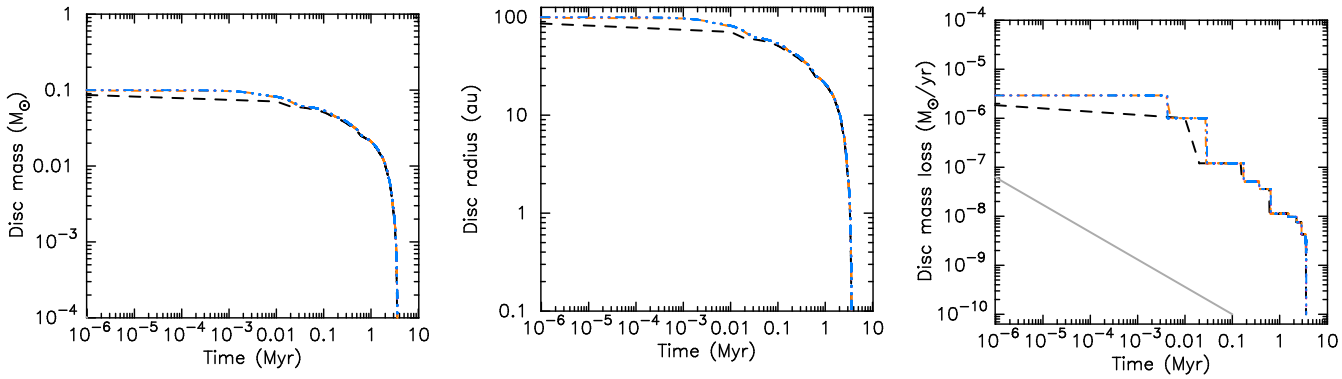

(a) Disc mass (b) Disc radius (c) Mass loss rate

Figure A1. Evolution of a single disc in a radiation field where the disc radius is allowed to evolve according to equation (7). In this simulation the radiation field is $10^4 G_0$, the stellar mass is 1 $M_\odot$, the initial disc mass is 0.1 $M_\odot$ and the initial disc radius is 100 au. We show the evolution of the disc mass in panel (a), the evolution of the disc radius in panel (b) and the mass-loss rate responsible for this evolution in panel (c). The solid grey lines are the results for a time-step of 0.1 Myr, the dashed black lines are 0.01 Myr, the dot–dashed orange lines are 0.001 Myr, the dotted pink lines are 10^{-4} Myr and the dot–dot–dot–dashed blue lines are 10^{-5} Myr.

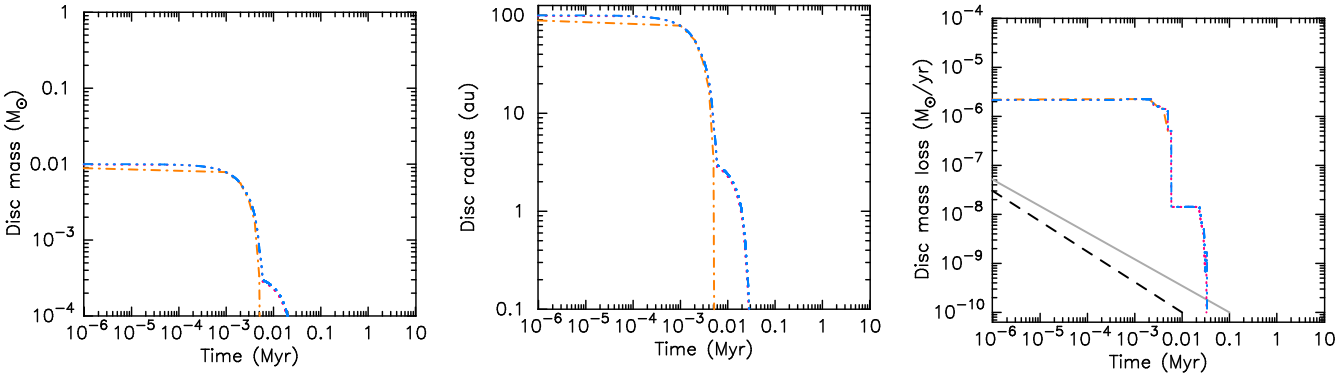

(a) Disc mass (b) Disc radius (c) Mass loss rate

Figure A2. Evolution of a single disc in a radiation field where the disc radius is allowed to evolve according to equation (7). In this simulation the radiation field is $10^4 G_0$, the stellar mass is 0.1 $M_\odot$, the initial disc mass is 0.01 $M_\odot$ and the initial disc radius is 100 au. We show the evolution of the disc mass in panel (a), the evolution of the disc radius in panel (b), and the mass-loss rate responsible for this evolution in panel (c). The solid grey lines are the results for a time-step of 0.1 Myr, the dashed black lines are 0.01 Myr, the dot–dashed orange lines are 0.001 Myr, the dotted pink lines are 10^{-4} Myr and the dot–dot–dot–dashed blue lines are 10^{-5} Myr.

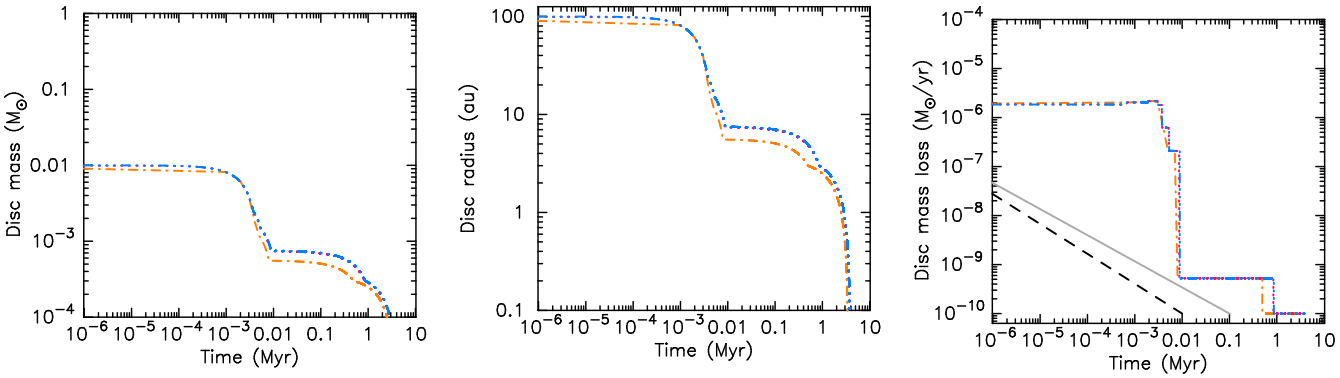

(a) Disc mass (b) Disc radius (c) Mass loss rate

Figure A3. Evolution of a single disc in a radiation field where the disc radius is allowed to evolve according to equation (7). In this simulation the radiation field is $10^3 G_0$, the stellar mass is 0.1 $M_\odot$, the initial disc mass is 0.01 $M_\odot$ and the initial disc radius is 100 au. We show the evolution of the disc mass in panel (a), the evolution of the disc radius in panel (b) and the mass-loss rate responsible for this evolution in panel (c). The solid grey lines are the results for a time-step of 0.1 Myr, the dashed black lines are 0.01 Myr, the dot–dashed orange lines are 0.001 Myr, the dotted pink lines are 10^{-4} Myr and the dot–dot–dot–dashed blue lines are 10^{-5} Myr.

black), 10^{-3} Myr (dot–dashed orange), 10^{-4} Myr (dotted pink), and 10^{-5} Myr (dot–dot–dot–dashed blue). In some plots of the disc mass and disc radius evolution (panels a and b), the black and grey lines are not shown because the values are immediately zero after the first time-step. In Fig. A1, we show the evolution of a 0.1 $M_\odot$ disc around a 1 $M_\odot$ star in a very strong ($10^4 G_0$) radiation field, where the initial disc radius is 100 au. In this simulation, the time-step of 0.1 Myr (the solid grey line) is far too coarse, and the disc is immediately destroyed. The versions of the simulation with the smaller time-steps converge, although there is some deviation when the time-step is 0.01 Myr (compare the dashed black lines to the other lines). This disc is destroyed altogether (i.e. the disc mass drops to zero) after 3.5 Myr in the convergent simulations.

If we keep the radiation field high ($10^4 G_0$) and the radius of the disc at 100 au, but decrease the mass of the host star to 0.1 $M_\odot$ and the mass of the disc to 0.01 $M_\odot$, then this disc is destroyed on much faster time-scales (0.03 Myr – see Fig. A2). Here, time-steps of 0.1 and 0.01 Myr are unsuitable, and there is some slight divergence between simulations where the time-step is 10^{-3} Myr and the two simulations where the time-step is lower.

Next, in Fig. A3 we reduce the radiation field to $10^3 G_0$, but keep all other parameters the same (the mass of the host star is 0.1 $M_\odot$, the mass of the disc is 0.01 $M_\odot$, and the disc radius is 100 au. In this simulation, again time-steps of 0.1 and 0.01 Myr are unsuitable, but there is better convergence between time-steps of 10^{-3} Myr and the two simulations where the time-step is lower. There is a slight difference in the temporal evolution of the discs (compare the orange dot–dashed lines to the blue and pink lines), but the disc is destroyed at the same time (2.9 Myr) for time-steps of 10^{-3} Myr and lower.

When we decrease the initial disc radius from 100 to 10 au, we also see convergence of the simulations for time-steps of 10^{-3} Myr and smaller, and these simulations are shown in Fig. A4 (for a host star mass 1 $M_\odot$ star and disc mass 0.1 $M_\odot$) and in Fig. A5 (for a host star mass 0.1 $M_\odot$ star and disc mass 0.01 $M_\odot$).

In summary, the disc evolution aspect of our simulations reaches reasonable convergence for time-steps of 10^{-3} Myr, and whilst an even smaller time-step would further increase the accuracy of the calculations, we deem it an unnecessary extra computational expense to do this.

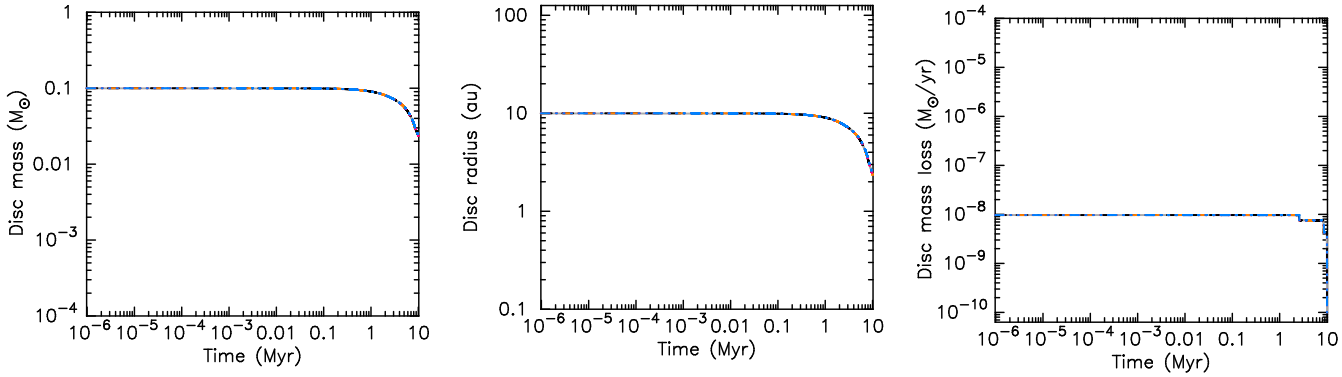

(a) Disc mass (b) Disc radius (c) Mass loss rate

Figure A4. Evolution of a single disc in a radiation field where the disc radius is allowed to evolve according to equation (7). In this simulation the radiation field is $10^4 G_0$, the stellar mass is 1 $M_\odot$, the initial disc mass is 0.1 $M_\odot$, and the initial disc radius is 10 au. We show the evolution of the disc mass in panel (a), the evolution of the disc radius in panel (b) and the mass-loss rate responsible for this evolution in panel (c). The solid grey lines are the results for a time-step of 0.1 Myr, the dashed black lines are 0.01 Myr, the dot–dashed orange lines are 0.001 Myr, the dotted pink lines are 10^{-4} Myr, and the dot–dot–dot–dashed blue lines are 10^{-5} Myr.

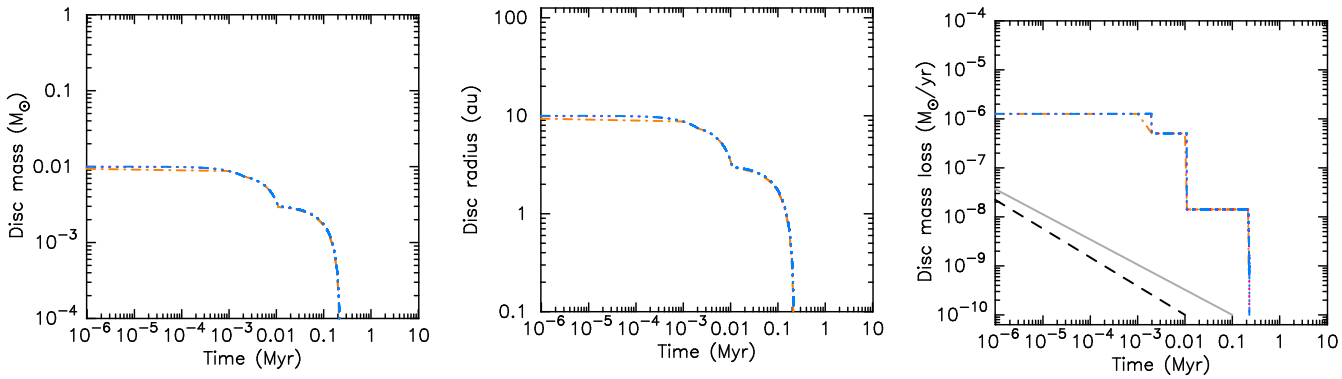

(a) Disc mass (b) Disc radius (c) Mass loss rate

Figure A5. Evolution of a single disc in a radiation field where the disc radius is allowed to evolve according to equation (7). In this simulation the radiation field is $10^4 G_0$, the stellar mass is 0.1 $M_\odot$, the initial disc mass is 0.01 $M_\odot$, and the initial disc radius is 10 au. We show the evolution of the disc mass in panel (a), the evolution of the disc radius in panel (b) and the mass-loss rate responsible for this evolution in panel (c). The solid grey lines are the results for a time-step of 0.1 Myr, the dashed black lines are 0.01 Myr, the dot–dashed orange lines are 0.001 Myr, the dotted pink lines are 10^{-4} Myr and the dot–dot–dot–dashed blue lines are 10^{-5} Myr.

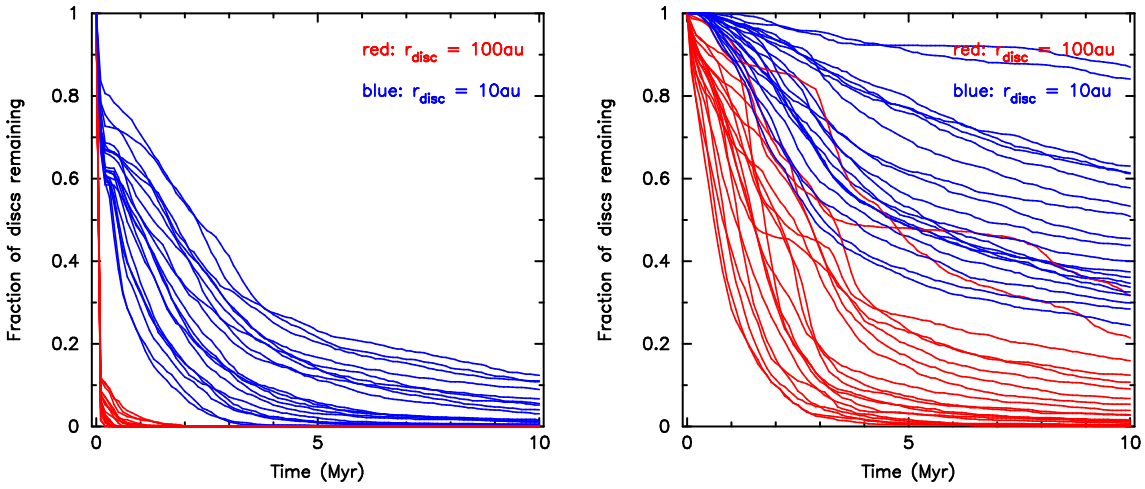

(a) FRIED grid, fixed disc radii, 100au

(b) Nicholson et al. (2019), fixed disc radii

Figure B1. Comparison of the evolution of disc fractions in our default simulation ($\tilde{\rho} = 100\,\mathrm{M}_\odot\,\mathrm{pc}^{-3}$, $D = 2.0$, $\alpha_{\rm vir} = 0.3$). with different prescriptions for the disc mass-loss due to photoevaporation. Both panels show the evolution of disc fractions in simulation where the discs have initial radii of 10 and 100 au. The left-hand panel shows the disc fractions when the mass-loss rates from the FRIED grid are adopted, with the disc radii fixed to their initial values. The right-hand panel shows the disc fractions when the FUV-induced mass-loss rates are determined from equation (B1) (Scally & Clarke 2001; Nicholson et al. 2019).

APPENDIX B: COMPARISON WITH PREVIOUS PHOTOEVAPORATION MODELS

Despite in some instances adopting very similar initial conditions for our star-forming regions to those in our previous work (Nicholson et al. 2019), we find that the mass-loss rates due to FUV photoevaporation in the FRIED grid models (Haworth et al. 2018b) are much higher. In Nicholson et al. (2019), the mass-loss due to EUV radiation is the same as that adopted here and by other authors (equation 5, e.g. Johnstone et al. 1998; Winter et al. 2019b), but we used the FUV photoevaporation mass-loss rate $\dot{M}_{\rm FUV}$ derived by Scally & Clarke (2001), which is *independent* of the distance to the ionizing star(s), d:

$$\dot{M}_{\rm FUV} \simeq 2 \times 10^{-9} r_{\rm disc}\ \mathrm{M}_\odot\,\mathrm{yr}^{-1}, \tag{B1}$$

where $r_{\rm disc}$ is the radius of the disc in au, as before. This more simplistic prescription appears to have severely underestimated the FUV mass-loss rate, as shown in Fig. B1. Here, we show the evolution of disc fractions in our default star-forming regions ($\tilde{\rho} = 100\,\mathrm{M}_\odot\,\mathrm{pc}^{-3}$, $D = 2.0$, $\alpha_{\rm vir} = 0.3$) and where the discs have initial radii of 10 and 100 au. In the left-hand panel the mass-loss is calculated with the FRIED grid, and the disc radii are kept constant (for a fairer comparison with Nicholson et al. 2019). In the right-hand panel we implement the FUV mass-loss according to equation (B1), as in Scally & Clarke (2001) and Nicholson et al. (2019).

This paper has been typeset from a TEX/LATEX file prepared by the author.